The effect of Mg concentration in silicate glasses on CO 2 solubility and solution mechanism: Implication for natural magmatic systems

Yann Morizet, Michael Paris, David Sifré, Ida Di Carlo, Fabrice Gaillard

Accepted Manuscript

The effect of Mg concentration in silicate glasses on CO_2 solubility and solution mechanism: Implication for natural magmatic systems

Yann Morizet, Michael Paris, David Sifré, Ida Di Carlo, Fabrice Gaillard

Please cite this article as: Morizet, Y., Paris, M., Sifré, D., Di Carlo, I., Gaillard, F., The effect of Mg concentration in silicate glasses on CO_2 solubility and solution mechanism: Implication for natural magmatic systems, *Geochimica et Cosmochimica Acta* (2016), doi: http://dx.doi.org/10.1016/j.gca.2016.11.006

The effect of Mg concentration in silicate glasses on CO$_2$ solubility and solution mechanism: Implication for natural magmatic systems.

Yann Morizet[1*], Michael Paris[2], David Sifré[3], Ida Di Carlo[3], Fabrice Gaillard[3]

(1) Université de Nantes, Nantes Atlantique Universités, Laboratoire de Planétologie et Géodynamique de Nantes (LPGN)

UMR CNRS 6112

2 rue de la Houssinière, 44322 NANTES (France)

(2) Institut des Matériaux Jean Rouxel (IMN), Université de Nantes

UMR CNRS 6502

2 rue de la Houssinière, BP32229, 44322 NANTES Cedex 3 (France)

(3) CNRS/INSU-Université d'Orléans – BRGM

UMR 7327

Institut des Sciences de la Terre d'Orléans

1a rue de la Férollerie, 45071, Orléans, France

1

Corresponding author: Yann Morizet

Postal address:

Laboratoire de Planétologie et Géodynamique de Nantes (LPG Nantes), UMR-CNRS 6112,

Université de Nantes.

2 rue de la Houssinière, 44322 Nantes Cedex (FRANCE)

phone: +33 (0) 2 5112 5491

fax: +33 (0) 2 5112 5268

[*]E-mail: yann.morizet@univ-nantes.fr

Abstract

Following an experimental approach conducted between 0.5 and 1.5 GPa, we investigated the change in CO_2 solubility as a function of the XMg (MgO/(MgO+CaO)) for a range of silicate glasses. The synthesised CO_2-bearing glasses have XMg up to 0.72, stoichiometric NBO/T (degree of polymerization) up to 2.6 corresponding to highly depolymerized compositions analogues to kimberlites. Several samples were synthesised with ^{17}O enrichment to investigate the CO_2 dissolution mechanism via the change in O species environments by NMR spectroscopy.

The experimental results show that CO_2 solubility increases with NBO/T in agreement with previous works. In addition, increasing XMg strongly decreases CO_2 solubility: from 18 to 7 wt.% CO_2 as XMg ranges from 0 to 0.6 (1.5 GPa and NBO/T ~ 2).

^{17}O NMR results demonstrate that CO_2 molecules dissolve as CO_3^{2-} groups showing a signal at +146 ppm for which the intensity is linearly correlated to the wt.% CO_2 determined by Raman. The analysis of the oxygen environments as a function of CO_2 content for Mg O^{NBO} (+62 ppm) and Ca O^{NBO} (+103 ppm) show that CO_2 dissolves preferentially in the vicinity of Ca^{2+} atoms. The difference in CO_2 solubility is explained by the ability for Mg^{2+} cations to act as a weak network former and to be present in four-fold coordination or by the stronger affinity of CO_2 molecules for Ca^{2+} rather than for Mg^{2+}. We show that the CO_2 solubility is negatively correlated to the melt ionic field strength which reflects the variation in the affinity of CO_2 molecules for one cation or another.

Strongly depolymerized mantle melts, such as kimberlites, melilitites, nephelinites and basanites will exhibit lower CO_2 solubility than currently assumed due to their high MgO content which must imply degassing at greater depth, potentially in the sub-lithospheric mantle.

1. Introduction

Carbon dioxide (CO_2) is a major component of silica undersaturated melts (Brey and Green, 1975; 1976; Thibault and Holloway, 1994; Brooker et al., 2001a; Dasgupta and Hirschmann, 2006; Dasgupta et al., 2007; Behrens et al., 2009; Morizet et al., 2014a; Moussallam et al., 2015). In particular, CO_2 is recognized to play a crucial role in the ascent of primary kimberlitic melts originating at depth (Becker and Le Roex, 2006; Sparks et al., 2006; Kopylova et al., 2007; Mitchell, 2008; Kjarsgaard et al., 2009; Brooker et al., 2011; Russell et al., 2012; Moussallam et al., 2015; Sharygin et al., 2015; Sokol and Kruk, 2015). Recent experimental investigation (Moussallam et al., 2015) attempted to reconstruct the CO_2 solubility in kimberlitic melts and its dependence on pressure; nevertheless, in their work, Moussallam et al. (2015) investigated compositions with high Ca content which are probably not representative of natural kimberlitic melt recognized to have a high Mg content (Kjarsgaard et al., 2009). As a result, capturing the dynamics of volatiles during kimberlite ascent through the mantle and the crust requires studying in detail the effect of melt compositions on CO_2 dissolution mechanisms. For instance, Morizet et al. (2014a) showed that the CO_2 solubility increases in silicate glasses when increasing the K_2O/K_2O+Na_2O ratio. Early work by Brey and Ryabchikov (1994) also showed that CO_2 solubility decreases with increasing $MgO/MgO+CaO$. Furthermore, all existing solubility models predicts that CO_2 solubility in silicate melts decreases as Ca is replaced by Mg (Dixon, 1997; Papale et al., 2006; Lesne et al., 2011; Iacono-Marziano et al., 2012), but it remains unclear how such an effect impacts low SiO_2-melts such as kimberlites, melilitites or nephelinites.

Whether CO_2 has a strong affinity for a particular cation is dependent on the CO_2 dissolution mechanisms. There has been a great deal of effort in conducting experimental investigations

4

to constrain the way CO_2 dissolves in silicate glasses. In low silica melt, CO_2 dissolves as carbonate groups (CO_3^{2-}; Mattey et al., 1990; Thibault and Holloway, 1994; Brooker et al., 2001a; Morizet et al., 2014a). However, the exact dissolution mechanism is uncertain. Inasmuch, the potential effect of CO_2 on the silicate network molecular structure (i.e. change in the degree of polymerization or not; Moussallam et al., 2016a) is not clear. Recent works (Morizet et al., 2015; Moussallam et al., 2016a) suggests that CO_2 forms free ionic carbonate clusters such as CO_3^{2-} M^{n+}. Brooker et al. (2001b) and Morizet et al. (2014a; 2015) suggests that CO_2 molecules might use available Non-Bridging Oxygen (NBO) present in the melt to form NBO-CO_3^{2-} M^{n+} units.

These hypotheses are commonly based on an incomplete spectroscopic viewpoint which is often dominated by the study of cations (e.g. ^{13}C MAS NMR). From a general standpoint, silicate melt structure has been widely studied using various spectroscopic approaches (e.g. Mysen et al., 1980; Greaves et al., 1981; Murdoch et al., 1985; Maekawa et al., 1991; Mysen, 1999) with the aim of determining the local arrangement of network formers or modifiers, for example, spectroscopic investigations aimed at determining the degree of polymerization. This degree of polymerization is often expressed in term of the parameter NBO/T corresponding to the ratio between the number ofNon-Bridging Oxygens and the number of tetrahedrally coordinated (i.e. network forming) cations (Mysen, 1988, 1990). However, the methods used (^{29}Si, ^{27}Al NMR; Raman) are indirect and the concentrations of the different oxygen species (Bridging Oxygens between network formers, BO; Non-Bridging Oxygen surrounded by network modifiers, NBO) cannot be readily extracted and the effect of CO_2 on NBO/T is still to be confirmed. Furthermore, free oxygen species (free O^{2-}) are also mentioned and observed in extremely low SiO_2 compositions (Nasikas et al., 2012; Nesbitt et al., 2015; Sawyer et al., 2015). Similarly, oxygen triclusters (threefold coordinated O atom, O^{III}) are also suggested to be present in silicate glass structures (Toplis et al., 1997; Stebbins

et al., 2001; Benoit et al., 2005; Iuga et al., 2005; Thompson and Stebbins, 2011).^{17}O NMR spectroscopy has revealed itself to be a powerful tool in describing the oxygen environments (BO, NBO, O^{III} and free O^{2-}) in silicate glasses in terms of environments bonded to the network former and network modifier cations (Farnan et al., 1992; Stebbins et al., 2001; Allwardt et al., 2003; Lee et al., 2004; Kelsey et al., 2008; Lee and Sung, 2008; Lee and Stebbins, 2009; Thompson and Stebbins, 2011; Nasikas et al., 2012; Jaworski et al., 2015). However, the direct influence of CO_2 on the different oxygen sites in silicate glasses is currently unexplored.

The role of network modifier cations (mostly Na^+, K^+, Ca^{2+} and Mg^{2+} in silicate glasses) is complex to comprehend as there is a strong interplay between those cations in the melt structure (Florian et al., 1996; Stebbins et al., 1997; Allwardt et al., 2003; Allwardt and Stebbins, 2004; Kelsey et al., 2008; Lee and Sung, 2008), inducing non-linear changes in the physical properties of melts (Neuville and Richet, 1991; Kjeldsen et al., 2013). The case of Mg^{2+} is interesting as this cation can adopt various structural roles in silicate glasses. Due to its higher cation field strength as compared to Ca^{2+}, Mg^{2+} has a lower coordination number (Shimoda et al., 2008; Cormier and Cuello, 2013), higher bond strength to oxygen and shorter Mg-O distance (Katz et al., 1996). In silicate glass, it has been demonstrated that Mg^{2+} can have coordination numbers from 4 to 6 (Ildefonse et al., 1995; Tabira, 1996; Wilding et al., 2004, 2012; Shimoda et al., 2008a,b; Sen et al., 2009; Cormier and Cuello, 2013), therefore suggesting that Mg^{2+} can act as a network modifier but also as a weak network former (the Mg-O bond strength in MgO_4 unit being considerably weaker than the bond strength of Si-O in SiO_4 unit, Kohara et al., 2011) when present in four-fold coordination. The existence of Mg^{2+} as a weak network former on CO_2 dissolution mechanism has not yet been investigated.

In the present work, we conducted an experimental study between 0.5 and 1.5 GPa using piston-cylinder apparatus to investigate the change in CO_2 solubility as a function of the XMg

(MgO/MgO+CaO) for a wide range of compositions: $0 < XMgO < 0.72$. We used ^{17}O MAS NMR spectroscopy to explain the change in CO_2 solubility as a function of XMg and hence provide information on the CO_2 dissolution mechanisms as a function of XMg in the investigated compositions. This work is part of a more global research programme aiming at determining 1) the exact CO_2 dissolution mechanisms as a function of silicate melt compositions and 2) the effect CO_2 induces on the silicate melt structure and its implication for physical properties of silicate melts.

2. Experimental synthesis

2.1. Starting material

The objectives of the present work are to investigate the change in CO_2 solubility as a function of XMg in the melt, investigate the possible structural reasons for the variability in CO_2 solubility, and extract from the results possible implications for low-SiO_2 silicate melts. As a result, we investigated several synthetic silicate glass compositions in the Na_2O-CaO-MgO-Al_2O_3-SiO_2 system. The major element composition for the synthesised glasses determined by Electron Probe Micro-Analysis (EPMA) is provided in wt.% in Table 1. In the investigated compositions, the SiO_2 ranges from 30 to 47 wt.%; Al_2O_3 ranges from 4 to 17 wt.%; MgO ranges from 0 to 22 wt.%; CaO ranges from 10 to 42 wt.%; and Na_2O is up 6 wt.%.

All the starting materials were prepared from a mixture of oxides (SiO_2, Al_2O_3, CaO and MgO) and carbonates ($CaCO_3$ and Na_2CO_3); the latter is used as the source for CO_2 during the experiments. As shown in Table 1, in all the experiments, CO_2 was present above saturation in the starting material. Before preparing the starting material, oxides and carbonates were dried for several hours at 1100 and 400°C, respectively; in order to reduce the adsorbed water.

7

RB8, HK and XE2 starting materials were also prepared with isotopically-doped oxides ($Si^{17}O_2$, $Al_2^{17}O_3$ with 40% ^{17}O elemental enrichment) for investigating the O speciation with ^{17}O NMR spectroscopy. Additionally, several samples (RB8E, HK and XE2) were also prepared with ^{13}C and ^{29}Si enrichment but those data are not presented in the purpose of this work. All the investigated compositions are Fe-free. The absence of iron is justified by the analytical need for NMR spectroscopy which cannot be conducted on Fe-bearing composition.

The investigated compositions exhibit a wide range of XMg values: RB8 composition has been prepared without MgO; X1 to X3 compositions have been prepared with a variable XMg from 0.25 to 0.72. All compositions are moderately to highly depolymerized expressed by the change in the NBO/T value from 1.0 to 2.6 calculated from chemical composition (the detail of the NBO/T calculation is described and given in Table 1). Compositions X1 to X3 have approximately the same degrees of polymerization (NBO/T ~ 1), while RB8 and HK have slightly different degree of polymerization, ~2 and ~2.6, respectively. However, we will show that such differences in NBO/T do not significantly affect the measured CO_2 solubility and that XMg has a more profound impact on CO_2 solubility. The choice of starting materials (constant NBO/T ~ 1 and 2) is made such that the effect of XMg on CO_2 solubility can be clearly identified.

2.2. High-pressure piston cylinder synthesis

Starting material was loaded and weighed into Pt capsules. All the experiments were conducted under anhydrous conditions. X1, X2 and X3 starting materials were loaded in 2.9 outer diameter Pt capsules and the three capsules were subsequently collated together into the high-pressure assembly; therefore those three compositions experienced the same pressure – temperature conditions. For RB8, HK and XE2 only a single 5 mm outer diameter capsule

8

was loaded into the high-pressure assembly. The Pt capsules were loaded in a 19 mm (3/4 inch) talc-pyrex assembly. The Pt capsules were surrounded by an alumina sleeve to prevent contact with the graphite furnace. A tapered graphite furnace was used in order to reduce the temperature gradient along the capsules (Morizet et al., 2002).

The high-pressure experiments were conducted in end-loaded piston-cylinder apparatus at pressure between 0.5 and 1.5 GPa and under super-liquidus conditions at 1525°C. The temperature during the experiments was monitored by a type B thermocouple ($PtRh_6$-$PtRh_{30}$) with an accuracy of ±5°C. We used a special design for the 3/4 inch pressure plate with holes drilled into the plate to ensure higher quench rate (>200°C/s; Morizet et al., 2015). The run duration was at least 30 min to ensure equilibrium (Mysen and Seitz, 1975; Jakobsson, 1997; Brooker et al., 1999), followed by an isobaric quench.

In most of the cases (except RB8 samples), the recovered sample consists in a clear glass, free of decompression bubbles or crystals. Besides, the capsule opening produced a hiss suggesting that the capsule was sealed and an excess fluid phase was present. Recovered samples of RB8E11 and RB8E12 experiments have a milky aspect and careful observation and characterization with Micro-Raman reveals the presence of $CaCO_3$ crystals which are attributed to quench crystals. The $CaCO_3$ crystal distribution is erratic and therefore cannot be attributed to experimental immiscibility between a silicate melt and carbonate melt (Martin et al., 2013). ^{27}Al-MAS NMR also reveals the presence of a small quantity of corundum crystals with a ^{27}Al NMR signal at +14 ppm. This signal has been observed in a totally clear glass and is attributed to an external pollution from the surrounding alumina sleeve when recovering the glass sample after opening the capsules.

3. Analytical techniques

3.1. Electron Probe Micro-Analyses

The major element compositions of glasses were determined using Electron Probe Micro-Analyses. Measurements were done on a Cameca SXFive©, at 15kV and 10 nA, with 10 s peak counting time for all elements. Na and K were analysed first. Analyses were conducted in defocused mode (20 µm beam diameter) in order to reduce any elemental loss. The average major elements concentrations for the synthesised glasses were obtained from more than 15 analyses. The determined glass composition is reported in Table 1 in wt.%. The standard deviation for each oxide does not exceed ±1 wt.%. We used the difference to 100% as an estimate of the volatile content in a similar way to Moussallam et al. (2015; see Table 1 and Supplementary material 1).

3.2. Vibrational spectroscopies

We used vibrational spectroscopies (Micro-FTIR and Micro-Raman) on the synthesised silicate glasses to quantify dissolved volatile species (H_2O and CO_2). Micro-Raman spectra were acquired on a Jobin-Yvon Labram spectrometer equipped with an Innova 300-5W Argon ion laser from Coherent© operating at a wavelength of 514 nm. The spectrometer is equipped with a 2400 grooves/mm grating allowing a spectral resolution on the order of 1 cm^{-1}. Analyses were performed in confocal mode (hole = 500 µm, slit = 200 µm), using a x50 Olympus objective. The spectral range covered was between 200 and 1350 cm^{-1}. The spectral frequency position was calibrated using the emission lines of Ne- and Hg-lamps with an accuracy within ±1 cm^{-1}. The output power was set to 125 mW. Several spectra were collected on each sample. The acquisition depth was optimized in order to obtain the highest Raman signal (Behrens et al., 2006; Mercier et al., 2009; Le Losq et al., 2012). We varied the acquisition time on a given sample (15 to 60 s) and up to 10 scans were acquired for each spectrum. The spectra were acquired at room temperature and no correction was applied for

the dependence of the scattered intensity on temperature and frequency (Neuville and Mysen, 1996; Long, 2002).

We used the method described by Morizet et al. (2013) to determine the CO_2 content via Raman spectroscopy. That calibration for CO_2 content is based on a linear calibration function of the form wt.% CO_2 = 15.17 x CO_3/HF relating the CO_2 content to the ratio between the area of the CO_3^{2-} peak and the high frequency envelop of the silicate glass vibrational signature (CO_3/HF). The calibration function has been updated (89 data points and CO_2 content up to 23 wt.%) and the linear relationship is wt.% CO_2 = 13.5 x CO_3/HF. The detail of this updated calibration is provided in Supplementary material 1 and 2. Typical Raman spectra simulations are shown in Figure 1 and the whole set of simulation for each sample is provided in Supplementary material 1 and 2.

We conducted Micro-FTIR analyses on the recovered high-pressure glasses to determine the H_2O content. Analyses were conducted on a ThermoFisher FTIR5700 equipped with a Continuµm© microscope. We used a CaF_2 beamsplitter, a MCT-B detector and IR light to acquire the FTIR spectra in the 4000-6000 cm^{-1} region for determining the OH^- (4500 cm^{-1}) and H_2O^{mol} (5200 cm^{-1}) concentrations. The concentration of each species was determined with the Beer-Lambert law (Ihinger et al., 1994; Ohlhorst et al., 2001). In the Beer-Lambert law, the species concentration is a function of the sample density, sample thickness and extinction coefficient (ε_i) of the measured species (OH^- and H_2O^{mol}). We measured the thickness of the sample using a Mitutoyo© digitometer with an accuracy of ±1 µm. We used density values calculated from the chemical composition with the model of Lange and Carmichael (1990) which includes the change in oxides partial molar volume as a function of pressure and temperature. Density calculations were conducted at the pressure and temperature at which the samples are synthesised. Although this density model calculation is applied for liquid; Guillot and Sator (2007) showed that the change in density in between

11

liquid and glass is small (~10% in relative) towards an increase in density from the liquid to the glass. Therefore, the derived H_2O content with Beer-Lambert law will represent a maximum. As the OH^- and H_2O^{mol} extinction coefficient values are a strong function of the glass chemical composition (Ihinger et al., 1994; King et al., 2002), it was not possible to use an appropriate extinction coefficient value for the silicate glasses synthesised here. For low silica RB8 and HK, we used the linear extinction coefficient provided by Behrens et al. (2009) initially applied to Alban Hill phonotephritic glass: $\varepsilon_{OH} = 0.62$ L.mol^{-1}.cm^{-1} and ε_{H2Omol} = 1.02 L.mol^{-1}.cm^{-1}. For more silica rich compositions (X1, X2, XE2 and X3), we used the linear extinction coefficient reported by Mandeville et al. (2002) initially applied to Krakatau andesitic glass: $\varepsilon_{OH} = 0.89$ L.mol^{-1}.cm^{-1} and $\varepsilon_{H2Omol} = 1.46$ L.mol^{-1}.cm^{-1}. We choose those extinction coefficients as they were applied to glass compositions which are close to the ones studied here: depolymerized for phonotephritic glass (Behrens et al., 2009) and polymerized for andesitic glass (Mandeville et al., 2002); nevertheless, we are perfectly aware that the use of those extinction coefficients is not entirely appropriate. The H_2O^{tot} is the sum of the OH and H_2O^{mol} concentrations. For X1, X2 and X3, the H_2O^{tot} ranges from 0.2 to 1.2 wt.%. For the depolymerized synthesised glasses (RB8 and HK with NBO/T $\geq$ 2), the H_2O^{tot} ranges from 0.4 to 1.5 wt.% with a typical error better than 0.2 wt.%. The presence of water is due to adsorption of atmospheric H_2O onto the starting material prior to capsule preparation and sealing. The measured H_2O will induce a lower XCO_2 in the fluid phase but considering the strong excess in CO_2 during the experiments (see Table 1), we suggest that the presence of H_2O will not play a crucial role on the measured CO_2 solubility (e.g. Moussallam et al., 2016b).

3.3. Elemental analyses

Absolute measurement of the CO_2 content was done with a Thermo Scientific Flash 2000 CHNS elemental analyser. The elemental analyses was conducted on glasses with the aim to corroborate the CO_2 content determined using the Raman spectroscopic method. Although this analytical method is destructive, it has proven to be efficient in determining the CO_2 content in silicate glasses (Sifré et al., 2014; Moussallam et al., 2015; 2016b).

The elemental analyses were conducted only on a few samples for several reasons: 1) isotopically enriched samples are expensive and elemental analyses method is a destructive method and 2) elemental analyser is not able to quantify ^{13}C-bearing sample and can only detect ^{12}C isotope. The crushed glass sample (several mg) is loaded together with 1 mg of vanadium pentoxide in a tin capsule folded and analysed by combustion. The C released is combined to an O_2-flow through to form a CO_2 gas and subsequently analysed via an infrared cell. The analyser was calibrated prior to analysis. Replicated measurements (see Supplementary material 1) were conducted on each analysed sample to test the reproducibility of the analyses.

3.4. ^{17}O NMR spectroscopy

Solid State ^{17}O NMR (RB8E7, 11, 12, HK-1, -2 and XE2) was performed with a Bruker Avance III 500 MHz spectrometer. The ^{17}O spectra were referenced against liquid H_2O at 0 ppm.

The ^{17}O MAS NMR spectra were acquired with a 2.5 mm CP/MAS probe and a MAS frequency of 30 kHz. We used a full shifted echo acquisition ($\pi/12$-τ-$\pi/6$-acq) sequence with a pulse length of 1 µs for the $\pi/12$ pulse. The delay τ was set to 1.13 ms (rotor-synchronized). A recycle delay between scans of 2 s was determined to be sufficient to ensure complete relaxation of the ^{17}O spins.

4. Results

4.1. Raman spectra for CO_2-bearing silicate glasses

The Raman spectra obtained for the synthesised glasses (see Table 1) are shown in Figure 1. Silicate glass Raman spectra are shown for the experiments conducted on X1 to X3 compositions (NBO/T ~ 1) at 1.0 GPa (Figure 1A) and 1.5 GPa (Figure 1B). The Raman spectra for the experiment conducted on RB8 and HK compositions (NBO/T ~ 2) are shown in Figure 1C and D at 0.5 and 1.5 GPa, respectively. The Raman spectra are represented in the 750-1250 cm^{-1} spectral region showing the vibrational contributions of the symmetric stretch of the aluminosilicate network (ν_1 Q^n located between 850 and 1100 cm^{-1}; Mysen et al., 1982) and the symmetric stretch of the carbonate groups (ν_1 CO_3^{2-} at ~1080 cm^{-1}) dissolved in the framework of the aluminosilicate glasses (Morizet et al., 2013). No evidence for CO_2^{mol} groups has been observed in the spectral region of ~1390 cm^{-1} (White, 1974; Verweij et al., 1977; Sharma, 1979).

Under fluid saturated conditions (i.e. excess fluid during the experiments), it is clear from Figure 1 that increasing the XMg in the glass composition induces a decrease in the ν_1 CO_3^{2-} peak intensity. Considering that Raman spectra have been scaled so as to have a constant intensity in the ν_1 Q^n region, this change in the ν_1 CO_3^{2-} as a function of XMg reflects a change in the CO_2 content with changing XMg in the glass composition. As such, this change in peak intensity indicates that CO_2 solubility decreases with increasing XMg.

The CO_2 values derived from the CO_3/HF are reported in Figure 1 along with the Raman spectra. The entire set of Raman spectra simulations with the determined CO_3/HF values are provided in Supplementary material 1 and 2. In Figure 1A, for X1 to X3 glass compositions, at 1.0 GPa, for XMg = 0.24, the CO_2 solubility is 5.0 wt.% and decreases to 1.2 wt.% at XMg

= 0.72. In Figure 1B, at 1.5 GPa, the CO_2 solubility is changing from 7.5 to 1.5 wt.% CO_2 for

XMg between 0.24 and 0.72. The increase in CO_2 solubility with increasing pressure is

consistent with previously published data (Fine and Stolper, 1986; Thibault and Holloway,

1994; Brooker et al., 1999; Morizet et al., 2002).

For the more depolymerized compositions (RB8 and HK), we observe a higher CO_2

solubility. At 0.5 GPa, for RB8E7 and HK-2 glasses (Figure 1C), we determined a CO_2

solubility of 6.5 and 2.9 wt.% CO_2, respectively. The change in CO_2 solubility with increasing

NBO/T (from 1.0 to 2.6), regardless of the XMg value is in agreement with previous work

(Brooker et al., 2001a; Iacono-Marziano et al., 2012; Shishkina et al., 2014).

4.2. Change in CO_2 solubility monitored by ^{17}O MAS NMR

We show in Figure 2 the ^{17}O NMR spectra acquired in the MAS dimension for RB8, HK and

XE2 glasses. The ^{17}O NMR spectrum consists in two prominent peaks for RB8 samples with

peak maxima located at ~+40 and ~+100 ppm whereas only a single asymmetric peak is

observed for HK and XE2 samples with a peak maximum located at ~+50 ppm. For RB8

glass samples, the peak located at ~+100 ppm is assigned to the Ca O^{NBO} environments; the

peak located at ~+40 ppm is assigned to the T-O^{BO}-T environments where T is Si or Al atoms.

This peak is a combination of several individual contributions, principally Si-O^{BO}-Si with

weak contribution of Si-O^{BO}-Al due to the low Al content in the synthesised glasses (see

Table 1). It should be mentioned that the existence of Al-O^{BO}-Al clusters is energetically not

favoured due to the Al avoidance principle (Lee and Stebbins, 2002; Lee et al., 2010, 2015).

These two assignments are consistent with previous works on Ca-bearing silicate glasses

(Stebbins et al., 1997; Lee and Stebbins, 2003; Allwardt and Stebbins, 2004; Lee and

Stebbins, 2006; Kelsey et al., 2008; Lee and Sung, 2008). For HK and XE2 glass samples

which are a mixed Ca-Mg silicate glass composition (see Table 1), we observe a broad peak

located at ~+50 ppm corresponding to a complex convolution of several individual contributions. We observe a shoulder at higher ^{17}O ppm chemical shift (~+100 ppm) assigned to Ca O^{NBO} environments. Previous NMR investigations on Mg-bearing silicate glasses (e.g. Allwardt and Stebbins, 2004; Kelsey et al., 2008; Lee et al., 2015) demonstrated that there is a strong overlap between the T-O^{BO}-T and Mg O^{NBO} peak contributions at ~+40 ppm and ~+70 ppm, respectively.

We also identify two weak broad shoulders located at a ^{17}O chemical shift above ~+140 ppm and ~-25 ppm. Those two peaks are weak in intensity and not clearly resolved from Figure 2; however, those two species are required for the relevant spectrum deconvolution discussed in section 5.2. The broad peak at ~-25 ppm is weak in intensity but appears more prominent in Mg-rich composition compared to Ca-rich ones. This ~-25 ppm peak position is consistent with a possible attribution to oxygen atoms in tricluster configuration in which an oxygen atom is linked to three tetrahedra (Stebbins et al., 2001; Kubicki and Toplis, 2002; Iuga et al., 2005).

As observed in RB8E ^{17}O NMR spectra, the peak centred at ~+140 ppm appears to increase in intensity with increasing CO_2 content. This is less obvious for HK and XE2 spectra due to the lower CO_2 content (between 2.9 and 7.1 wt.% CO_2). We assign this peak to CO_3^{2-} environments in the silicate glass (see Section 5.2). This assignment agrees with the reported ^{17}O isotropic chemical shift for carbonate groups in liquids (Klemperer, 1978; and references therein) with two different ^{17}O isotropic chemical shifts at +155 and +220 ppm depending on the molecular configuration of the CO_3^{2-} group. As for crystalline solids, Smith et al. (1995) reports a ^{17}O isotropic chemical shift at +204 ppm for crystalline $CaCO_3$. Although, we identified in the recovered RB8E-11 and RB8E-12 crystalline $CaCO_3$, we do not observe any evidence of this $CaCO_3$ in Figure 2 suggesting that the $CaCO_3$ crystals are in low abundance.

In Figure 2, we observe that with the lowest CO_2 content (RB8E7 6.5 wt.% CO_2), the Ca O^{NBO} peak intensity is higher than the (Si,Al)-BO whereas at the highest CO_2 content (RB8E11 18.0 wt.% CO_2), the Ca O^{NBO} peak intensity is almost equal to the intensity of the T-O^{BO}-T. Hence upon CO_2 dissolution, there is a decrease in the ~+100 ppm Ca O^{NBO} peak accompanied by an increase in the ~+140 ppm CO_3^{2-} peak suggesting that CO_2 dissolves in the vicinity of Ca O^{NBO} units. Alternatively, the T-O^{BO}-T peak at ~+40 ppm increases due to the T-O^{BO}-T bridges formed upon CO_2 dissolution consistent with a polymerizing effect of CO_2 on silicate glass structure (Moussallam et al., 2016a).

5. Discussion

5.1. CO_2 solubility as a function of XMg

We show in Figure 3, the change in CO_2 solubility as a function of XMg for the synthesised glasses (see Table 1). For consistency and clarity, only the CO_2 content determined by Raman spectroscopy is considered. The CO_2 solubility data have been categorized as follows: CO_2 solubility is represented for a given pressure between 0.5 and 1.5 GPa; the change in CO_2 solubility for a given degree of polymerization is also differentiated: NBO/T ~ 1.0 for X1 to X3 glasses in Figure 3A, NBO/T ~2 for HK and RB8 glasses in Figure 3B. We also added to Figure 3B CO_2 solubility data points (RB38 and RB42) from Brooker et al. (2001a) obtained at 1.5 GPa and for glass compositions with NBO/T ~ 2 and having an XMg ~ 0.26. The reported CO_2 solubility is 14.0 and 14.8 wt.% for RB38 and RB42, respectively (Brooker et al., 2001a). We also added the CO_2 solubility data point obtained on RB8 composition by Brooker et al. (2001a) at 1.5 GPa; equivalent to the RB8 composition investigated in the present study. We observe that the CO_2 solubility determined in our RB8 composition at 1.5

GPa (RB8-1 and RB8E-11) is slightly higher (17.1 and 18.0 wt.% CO_2) than the CO_2

solubility determined in Brooker et al. (2001a; 15.6 wt.% CO_2) but remains within error.

As indicated in Figure 3, increasing the XMg in the glass induces a strong decrease in CO_2

solubility. For instance, at 1.5 GPa and for glass compositions having a NBO/T ~ 1, there is a

decrease in CO_2 solubility from 7.5 wt.% at XMg = 0.25 to 1.5 wt.% at XMg = 0.72. At

identical pressure, for glass compositions having a NBO/T ~ 2.0, the decrease in CO_2

solubility is also important with increasing XMg: ~17 wt.% CO_2 at XMg = 0 and 7.1 wt.%

CO_2 at XMg = 0.58. With a similar change in XMg (ΔXMg~0.5), the change in CO_2

solubility is different as a function of the degree of polymerization. If we consider the rate of

CO_2 solubility change as a function of XMg, we obtain the solubility decrease rate of ~0.5

and 1 wt.% CO_2 when XMg changes by 0.1 unit at NBO/T ~ 2 and ~ 1, respectively. In other

word, the CO_2 solubility is more sensitive to the XMg at lower NBO/T than at higher NBO/T.

The impact of this result will be discussed further in section 5.4; however, it can be easily

conceived that such a result will have a dramatic impact on the CO_2 solubility in Mg-rich

silicate melt compositions such as komatiites or kimberlites.

5.2. CO_2 signal from ^{17}O NMR spectra.

From the ^{17}O NMR spectra in Figure 2, we propose an assignment of the ~+140 ppm peak to

CO_3^{2-} species. In the present state we prefer to assign the +140 ppm peak to CO_3^{2-} groups

since 1) the nature of carbonate groups is probably of different kinds (i.e. free ionic

carbonates or carbonates connected to non-bridging oxygens; see Morizet et al., 2015) and 2)

there is no relevant literature on the present NMR signal. This assignment is corroborated by

the results shown in Figure 4 and 5. We present in Figure 4 a typical deconvolution of the [17]O

MAS NMR spectrum for RB8E-7, HK-1 and XE2-2 (Figure 2). We chose RB8E-7 and HK-1

samples as they have a comparable CO_2 content (6.5 and 7.1 wt.%, respectively); even though

they have been synthesised at different experimental pressure (0.5 GPa for RB8E7 and 1.5 GPa for HK-1). The deconvolution for all the ^{17}O spectra was conducted using Gaussian lines: four Gaussians for RB8E and five Gaussians for HK and XE2. Although ^{17}O is a quadrupolar nucleus, the use of Gaussian peaks is justified by the fact that the O sites are mainly controlled by the chemical shift distribution and second order quadrupolar interactions have only a limited impact on the peak line shape (Kelsey et al., 2008; Nasikas et al., 2012). The four Gaussian lines for RB8E take into account the presence of bridging oxygen species ($Si-O^{BO}-Al$, $Si-O^{BO}-Si$), one non-bridging oxygen species ($Ca\ O^{NBO}$), one corresponding to oxygen tricluster species ($O^{III\ BO}$) and one C-related species (CO_3^{2-}). The HK-1 decomposition takes into account the presence of an additional line related to the $Mg\ O^{NBO}$ non-bridging oxygen species.

The deconvolution approach for HK and XE2 ^{17}O spectra is probably simplistic considering that in these glass compositions an important intermixing is expected in between alkaline-earth and/or alkali cations (Lee and Stebbins, 2003; Allwardt and Stebbins, 2004; Lee et al., 2005; Kelsey et al., 2008; Lee and Sung, 2008; Nasikas et al., 2012; Pedone et al. 2012). Hence, the distinction between the non-bridging oxygen sites (e.g. 3Ca, 2Ca1Mg, 1Ca2Mg and 3Mg) was not done in the deconvolution procedure. Hence, the strong mixing between alkaline-earth cations prevents the determination of the XMg value from the simple decomposition of the ^{17}O NMR spectrum presently used (Allwardt and Stebbins, 2004).

The ^{17}O NMR spectra fitting parameters are reported in Table 2. The $T-O^{BO}-T$ has an average δ_{iso} = +41.3 ±5.0 ppm; the $Ca\ O^{NBO}$ has average δ_{iso} = +103.4 ±2.5 ppm; the $Mg\ O^{NBO}$ has average δ_{iso} = +67.5 ±2.3 ppm; the $O^{III\ BO}$ has an average δ_{iso} = -24.1 ±5.2 ppm and the CO_3^{2-} has average δ_{iso} = +145.8 ±1.9 ppm. Those peaks are relatively well-constrained considering the associated error on the δ_{iso} and the average δ_{iso} value is in agreement with previous work (Kelsey et al., 2008; Lee and Sung, 2008).

We show in Figure 5 the change in the X CO_3^{2-} as derived from the +146 ppm peak

determined from ^{17}O NMR spectra deconvolution (Table 2) as a function of XCO_2 determined

by Raman spectroscopy. The XCO_2 Raman is calculated from the major element oxides and

CO_2 content in wt.% shown in Table 1. We used a linear function to fit the evolution of the

XCO_3^{2-} ^{17}O NMR as a function of the XCO_2 obtained by Raman:

$$XCO_3^{2-} \, ^{17}O \, NMR = 0.838 \times XCO_2^{Raman} \quad \text{Eq. 2}$$

In this equation, the derived standard deviation is ±0.019 which corresponds to ±0.83 wt.%

CO_2. An important conclusion drawn from the linear trend in Figure 5 is that it confirms the

assignment of the +146 ppm peak to CO_3^{2-}-related species. We expected a slope close to 1 in

this correlation. A possible explanation for the slope of 0.8 is that the XCO_3^{2-} ^{17}O NMR is

underestimated. This underestimation might reflect several CO_3^{2-} environments consisting of

that contributing to the peak at +146 ppm and an additional unidentified one. This hypothesis

is consistent with the fact that several dissolution mechanisms for CO_2 as CO_3^{2-} are invoked

(Fine and Stolper, 1985; Kohn et al., 1991; Kubicki and Stolper, 1995; Tossell, 1995; Brooker

et al., 1999, 2001b; Morizet et al., 2014a, 2015).

5.3. The lack of affinity of CO_2 for Mg, as evidenced by ^{17}O NMR spectroscopy.

The stronger CO_2 affinity for Ca O^{NBO} than for Mg O^{NBO} can be deciphered spectroscopically

from the deconvolution in Figure 4. As shown in Table 1, the XE2 and HK chemical

compositions have been prepared with $XMg = 0.50$ and 0.58, respectively. Therefore, if CO_2

were to have no particular affinity for one cation or another, the peaks for Ca O^{NBO} and Mg

O^{NBO} species should have more or less equal intensities. This appears not to be the case from

the HK-1 deconvolution spectrum in Figure 4B in which the Mg O^{NBO} peak is more intense

than the Ca O^{NBO} peak. This difference strongly suggests that CO_2 dissolves preferentially in

the vicinity of the Ca atoms. From the ^{17}O NMR spectra point of view, the CO_2 dissolution

will induce a decrease in the intensity of the Ca O^{NBO} environment at +103 ppm whereas the intensity of the Mg O^{NBO} environment at +68 will remain unaffected. At the same time, CO_2 dissolution implies the formation of CO_3^{2-} groups associated to Ca^{2+} cations, giving rise to a peak at ~+146 ppm. Therefore, the decrease in the Ca O^{NBO} peak intensity at ~+103 ppm is accompanied by an increase in the intensity of the CO_3^{2-} peak at ~+146 ppm.

One possible explanation of the stronger affinity of CO_2 for Ca^{2+} environments might be explained by the structural role of Mg^{2+} in silicate glasses. It has been suggested that Mg^{2+} in silicate glasses can be in fourfold (Tabira, 1996; Wilding et al., 2004), fivefold (Ildefonse et al., 1995; Li et al., 1999) or sixfold coordinated (Kroeker and Stebbins, 2000). Work by Shimoda and co-workers (Shimoda et al., 2007, 2008a) based on ^{25}Mg NMR proposed that Mg^{2+} is present with several coordination number from 4 to 6, although the distinction of each coordination environment cannot be clearly made from ^{25}Mg NMR (Shimoda et al., 2008b). In solids, there is evidence that Mg^{2+} atoms have a lower coordination number than Ca^{2+} atoms (Katz et al., 1996; Sen et al., 2009). Therefore, Mg^{2+} acts as a network modifier but also as a weak network former (Kohara et al., 2004; Shimoda et al., 2007; Kalampounias et al., 2009; Nasikas et al., 2011; Kjeldsen et al., 2013) in a similar way to Si^{4+} or Al^{3+} cations. Considering that CO_2 is strongly affected by the concentration of network former cations (the higher the concentration of network former, the lower is the NBO/T and the lower the CO_2 solubility); it is perfectly conceivable that the presence of MgO_4 units as a network former induces the lower CO_2 solubility observed in Figure 4 for Mg-rich glass compositions. The current method to calculate the NBO/T assumes that Si^{4+} and Al^{3+} are the only network forming cations and Ca^{2+} and Mg^{2+} are considered as network modifier or charge compensating cation. This method is highly approximative as it does not take into account the possibility for Al^{3+} to be in five- or six-fold coordination nor does it integrate the possibility for Mg^{2+} to be in four-fold coordination. Unfortunately, no study is available to quantify in a

21

systematic way the existence of highly coordinated Al^{3+} or four-fold coordinated Mg^{2+} for a wide range of silicate melt composition. Furthermore, the effect of highly coordinated Al^{3+} or four-fold coordinated Mg^{2+} on CO_2 solubility is currently unknown.

5.4. The CO_2 solubility as a function of the Ionic Field Strength.

Alternatively, the variable CO_2 solubility might be explained by the energy difference between Mg^{2+} and Ca^{2+} cations. This difference is often considered in terms of the difference in cation field strength corresponding to the ratio between the charge and the square of its radius (z/r^2). It appears that silicate melt properties are often related to z/r^2. Recent work by Lee et al. (2015) showed that the degree of Al avoidance is strongly controlled by the z/r^2. Kelsey et al. (2009) showed that both the Al coordination number and the density of silicate melts are positively correlated to the modifier field strength. Malfait et al. (2007) related the ^{29}Si chemical shift to the ionic field strength and Davis et al (2011) showed that the Q^n species distribution in silicate glasses is controlled by the cation potential.

A possible relationship between the cation field strength and CO_2 solubility has not been demonstrated. For the network modifier cations, the z/r^2 is decreasing from Mg^{2+} to Ca^{2+} (3.9 and 1.7 for Mg^{2+} and Ca^{2+}, respectively) then followed by Na^+ (0.8) and K^+ (0.5). Morizet et al. (2014a) have shown that CO_2 solubility is higher in K_2O-rich than in Na_2O-rich silicate glasses. Consequently, we expect an increase in CO_2 solubility from Mg-rich to K-rich silicate melt compositions. The negative correlation in between CO_2 solubility and cation field strength is also corroborated by the fact that Si^{4+} and Al^{3+} have by far the highest cation field strength with $z/r^2 = 34.6$ and 13.58, respectively. Increasing Si content in silicate melt induces a decrease in CO_2 solubility. We have combined the previous information into a single parameter called Melt Ionic Field Strength (Melt IFS) which is defined as follow:

$$Melt\ IFS = \frac{\sum_i X_i \times {z_i}/{r_i^2}^{Cation}}{X_{O^{2-}} \times {|z_{O^{2-}}|}/{r_{O^{2-}}^2}}$$ Eq. 3

Where X_i and X_{O2^-} are the molar fraction of the i cation and O^{2-}. The z_i/r^2 represents the cation field strength and $|z_{O2^-}|/r^2$ the absolute value of the O^{2-} field strength. Therefore, the Melt IFS includes the energy difference in between the cations and incorporates the differential affinity of CO_2 molecules for one cation or another. Furthermore, the Melt IFS also includes the effect of the oxygen species (i.e. BO or NBO) on the CO_2 solubility.

We applied our approach to a set of selected experimental studies in the pressure range from 0.5 to 2.0 GPa (see Supplementary material 2 for the entire description of the experimental dataset). We considered CO_2 solubility experimental data from Brey and Green (1976) on olivine-melilitite; Mattey et al. (1990) on sodamelilite; Brey et al. (1991) on olivine melilitite; Pan et al. (1991) on alkali basalt; Thibault and Holloway (1994) on olivine-leucitite; Jakobsson (1997) on icelandite; Brooker et al. (2001a, b; 2011), Brooker and Kjarsgard (2011) on various natural and synthetic silicate glass compositions; Morizet et al. (2002) on haplophonolite; Shishkina et al. (2010) on tholeiitic basalt; Shishkina et al. (2014) on various natural mafic compositions (most of the CO_2-bearing silicate glasses in Shishkina et al., 2014; are also hydrated); Morizet et al. (2015) on haplobasalt; Moussallam et al. (2015, 2016b) on haplo-kimberlite. This dataset represents 90 CO_2 solubility data points between 0.5 and 2.0 GPa with CO_2 from 0.3 to 20.7 wt.%. This dataset covers a wide compositional range with NBO/T ranging from 0.2 for the haplophonolite (Morizet et al., 2002) to 3.3 for the olivine-melilitite (Brey et al., 1991); corresponding to a range in composition from slightly depolymerized to highly depolymerized. The Melt IFS varies from 7.53 for RB440 (Brooker et al., 2001a) to 11.08 for haplophonolite (Morizet et al., 2002).

23

We also took into consideration existing natural CO_2 contents measured in natural kimberlite rocks. One of the most complete databases has been reported in Kjarsgaard et al. (2009). The work of Kjarsgaard et al. (2009) gives major element composition and volatile content (CO_2 and H_2O) measured in natural kimberlitic supposed to be 'uncontaminated'. The investigated natural kimberlite composition is also provided in the Supplementary material 2. In these natural kimberlites, CO_2 goes up to 19.6 wt.%. The major element is expressed in the Na_2O-K_2O-CaO-MgO-Al_2O_3-SiO_2 system composition.

The evolution of the CO_2 solubility as a function of the Melt IFS is shown in Figure 6. As inferred earlier, we observe a negative correlation in between CO_2 solubility and calculated Melt IFS for the experimental data and showing a continuum between kimberlite and basalt silicate melts. There is a large scatter in this negative correlation probably suggesting that this representation is still too simplistic to account for the many parameters playing a role on silicate melt CO_2 solubility. The effect of pressure on CO_2 solubility is not visible in Figure 6 which might reflect a stronger control of the melt chemistry as compared to pressure control on CO_2 solubility. The existence of a CO_2 solubility continuum in between kimberlite and basalt also induces the dichotomy in two fields: high Melt IFS – high CO_2 and low Melt IFS – low CO_2. We consider that the negative trend represents a maximum of CO_2 solubility at a given melt IFS (i.e. composition). Hence, it would be impossible to generate CO_2 content data above this trend. Increasing pressure to increase CO_2 solubility would result in two liquids immiscibility (Brooker, 1998): coexistence of a carbonate liquid with a silicate liquid. On the contrary, CO_2 content below this trend is possible as shown by most of the data points for the natural kimberlites in Figure 6. It implies that most of the natural kimberlites have undergone degassing process lowering the CO_2 content.

The hypothesis of CO_2 degassing in kimberlites melts has been suggested by previous works (e.g. Sparks et al., 2006). This degassing might be due to a gradual change in the kimberlite

24

melt composition. It is commonly assumed that kimberlitic melt can be generated from a parental carbonatitic melt obtained from melting of a CO_2-bearing peridotite in the asthenosphere (Canil and Scarfe, 1990; Gudfinnsson and Presnall 2000; Russell et al., 2012; Sokol et al., 2015; Massuyeau et al., 2015). Russell et al. (2012) suggests that with subsequent dissolution of orthopyroxene ($MgSiO_3$) into the parental melt, there is a gradual evolution of the chemical composition towards kimberlitic melt composition. Russell et al. (2012) proposed that the progressive dissolution of $MgSiO_3$ induces a strong CO_2 degassing due to the progressive enrichment in SiO_2 in the melt; therefore ensuring adequate buoyancy of the melt to ascend through the lithosphere. Based on the present CO_2 solubility results, we show that the progressive enrichment in MgO has a similar effect to SiO_2 and leads to substantial additional CO_2 degassing. For instance, the highest CO_2 content measured in natural kimberlite is 19.6 wt.% at a Melt IFS = 7.02. For this data point (Canada K5A, see Supplementary material 2), the composition has a XMg = 0.55. The assimilation of 20% $MgSiO_3$ component will increase the XMg to 0.61 and the Melt IFS to 7.79. In Figure 6, such a change in the Melt IFS will induce a decrease in CO_2 solubility by almost 6 wt.%. Such CO_2 degassing could enhance melt buoyancy and trigger fast kimberlite ascent rate (Russell et al., 2012).

6. Summary

In the present work, we have conducted an experimental study between 0.5 and 1.5 GPa on a range of silicate melt compositions equilibrated at high temperature above melting temperature in presence of CO_2.

The newly obtained CO_2 solubility experimental data show that there is a strong control of the MgO/(MgO+CaO) (XMg) on the CO_2 solubility in silicate glass. The increasing XMg in

25

silicate glasses induces a decrease in CO_2 solubility. This result is also confirmed by ^{17}O MAS NMR spectroscopy. ^{17}O NMR spectra show that there is a gradual decrease in the abundance of Ca O^{NBO} species as compared to Mg O^{NBO} species with increasing CO_2 content suggesting that CO_2 molecules preferentially dissolve near Ca^{2+} cations. One structural hypothesis for this change is the possibility for the Mg^{2+} cation to be present in MgO_4 and acting as a weak network former. Another hypothesis for this change is the difference in between the Mg^{2+} and Ca^{2+} cation field strength (z/r^2). We show that increasing the global ionic field strength expressed by the Melt IFS induces a strong decrease in CO_2 solubility.

The present results have strong implications for the CO_2 solubility in natural magmatic systems. At a given pressure and SiO_2 content, Ca-rich silicate melts composition (e.g. melilitites) will dissolve more CO_2 than Mg-rich silicate melts composition (e.g. kimberlites) For these natural compositions, the expected change in CO_2 solubility is potentially large; and Ca-rich melts can dissolve twice as much CO_2 compared to equivalent Mg-rich melts.

References

Allwardt J. R., Lee S. K. and Stebbins J. F. (2003) Bonding preferences of non-bridging O atoms: Evidence from ^{17}O MAS and 3QMAS NMR on calcium aluminate and low-silica aluminosilicate glasses. *Am. Mineral.* **88**, 949-954.

Allwardt J. R. and Stebbins J. F. (2004) Ca-Mg and K-Mg mixing around non-bridging O atoms in silicate glasses: an investigation using ^{17}O MAS and 3QMAS NMR. *Am. Mineral.* **89**, 777-784.

Arndt N. T., Barnes S. J. and Lesher C. M. (2008) Komatiite. Cambridge University Press, U.K, pp. 488.

Becker M. and Le Roex A. P. (2006) Geochemistry of South African on- and offcraton, group I and group II kimberlites: Petrogenesis and source region evolution. *J. Petrol.* **47**, 673-703.

Behrens H., Roux J., Neuville D. R. and Siemann M. (2006) Quantification of dissolved H_2O in silicate glasses using confocal microRaman spectroscopy. *Chem. Geol.* **229**, 96–112.

Behrens H., Misiti V., Freda C., Vetere F., Botcharnikov R. E. and Scarlato P. (2009) Solubility of H_2O and CO_2 in ultrapotassic melts at 1200 and 1250°C and pressure from 50 to 500 MPa. *Am. Mineral.* **94**, 105-120.

Benoit M., Profeta M., Mauri F., Pickard C. J. and Tuckerman M. E. (2005) First-principles calculation of the ^{17}O NMR parameters of a calcium aluminosilicate glass. *J. Phys. Chem. B* **109**, 6052-6060.

Blichert-Toft J., Arndt N. T., Wilson A. and Coetzee G. (2015) Hf and Nd isotope systematics of early Archean komatiites from surface sampling and ICDP drilling in the Barberton Greenstone Belt, South Africa. *Am. Mineral.* **100**, 2396-2411.

Brey G. P. and Green D. H. (1975) The role of CO_2 in the genesis of olivine melilitites. *Contrib. Miner. Petrol.* **49**, 93-103.

Brey G. P. and Green D. H. (1976) Solubility of CO_2 in Olivine Melilitite at high pressures and role of CO_2 in the Earth's Upper mantle. *Contrib. Miner. Petrol.* **55**, 217-230.

Brey G. and Ryabchikov I. (1994) Carbon dioxide in strongly undersaturated melts and origin of kimberlitic magmas. *N. Jb. Miner. Mh.* **H10**, 449–463.

28

Brey G. P., Kogarko L. and Ryabchikov I. (1991) Carbon dioxide in kimberlitic melts. *N. Jb. Miner. Mh.* **H4**, 159–168.

Brooker R. A. (1998) The effect of CO_2 saturation on immiscibility between silicate and carbonate liquids: an experimental study. *J. Petrol.* **39**, 1905–1915.

Brooker R. A. and Kjarsgaard B. A. (2011) Silicate-Carbonate liquid immiscibility and phase relations in the system SiO_2-Na_2O-Al_2O_3-CaO-CO_2 at 0.1-0.25 GPa with applications to carbonatite genesis. *J. Petrol.* **52**, 1281–1305.

Brooker R. A., Kohn S. C., Holloway J. R., McMillan P. F. and Carroll M. R. (1999) Solubility, speciation and dissolution mechanisms for CO_2 in melts on the $NaAlO_2$-SiO_2 join. *Geochim. et Cosmochim. Acta* **63**, 3549-3565.

Brooker R. A., Kohn S. C., Holloway J. R., and McMillan P. F. (2001a) Structural controls on the solubility of CO_2 in silicate melts. Part I: Bulk solubility data. *Chem. Geol.* **174**, 225-240.

Brooker R. A., Kohn S. C., Holloway J. R. and McMillan P. F. (2001b) Structural controls on the solubility of CO_2 in silicate melts. Part II: IR characteristics of carbonate groups in silicate glasses. *Chem. Geol.* **174**, 241-254.

Brooker R. A., Sparks R. J. S., Kavanagh J. L. and Field M. (2011) The volatile content of hypabyssal kimberlite magmas: some constraints from experiments on natural rock compositions. *Bull. Volc.* DOI 10.1007/s00445-011-0523-7.

Canil D. and Scarfe C. M. (1990). Phase relations in peridotite + CO_2 systems to 12 GPa: implications for the origin of kimberlite and carbonate stability in the Earth's upper mantle. *J. Geophys. Res.* **95**, 15805–15816.

Cormier L. and Cuello G. J. (2013) Structural investigation of glasses along the $MgSiO_3$– $CaSiO_3$ join: Diffraction studies. *Geochim. et Cosmochim. Acta* **122**, 498-510.

Dasgupta R. and Hirschmann M. M. (2006) Melting in the Earth's deep upper mantle caused by carbon dioxide. *Nature* **440**, 659-662.

Dasgupta R., Hirschmann M. M. and Smith N. D. (2007) Partial melting experiments of peridotite + CO_2 at 3 GPa and genesis of alkalic ocean island basalts. *J. Petrol.* **48**, 2093-2124.

Davis M. C., Sanders K. J., Grandinetti P. J., Gaudio S. J. and Sen S. (2011) Structural investigations of magnesium silicate glasses by ^{29}Si 2D Magic-Angle Flipping NMR. *J. Non-Cryst. Solids* **357**, 2787-2795.

Dixon J. E. (1997) Degassing of alkalic basalts. *Am. Mineral.* **82**, 368–378.

Doweidar H. (1999) Density – structure correlations in silicate glasses. *J. Non-Cryst. Solids* **249**, 194-200.

Farnan I., Grandinetti P. J., Baltisberger J. H., Stebbins J. F., Werner U., Eastman M. A. and Pines A. (1994) Quantification of the disorder in network-modified silicate glasses. *Nature* **358**, 31-35.

Fine G. and Stolper E. (1985) The speciation of carbon dioxide in sodium aluminosilicate glasses. *Contrib. Mineral. Petrol.* **91**, 105–121.

Fine G. and Stolper E. M. (1986) Dissolved carbon dioxide in basaltic glasses: concentrations and speciation. *Earth Planet. Sci. Lett.* **76**, 263-278.

Florian P., Vermillion K. E., Grandinetti P. J., Farnan I. and Stebbins J. F. (1996) Cation distribution in mixed alkali disilicate Glasses. *J. Am. Chem. Soc.* **118**, 3493-3497.

Greaves G. N., Fontaine A., Lagarde P., Raoux D. and Gurman S. J. (1981) Local structure of silicate glasses. *Nature* **293**, 611-616.

Gudfinnsson G. H. and Presnall D. C. (2000) Melting behaviour of model lherzolite in the system CaO-MgO-Al$_2$O$_3$-SiO$_2$-FeO at 0.7-2.8 GPa. *J. Petrol.* **41**, 1241-1269.

Guillot B. and Sator N. (2007) A computer simulation study of natural silicate melts. Part I: Low pressure properties. *Geochim. et Cosmochim. Acta* **71**, 1249-1265.

Herzberg C. T. and O'Hara M. J. (1985) Origin of mantle peridotite and komatiite by partial melting. *Geophys. Res. Lett.* **12**, 541–544.

Iacono-Marziano G., Morizet Y., Le Trong E. and Gaillard F. (2012) New experimental data and semi-empirical parameterization of H$_2$O-CO$_2$ solubility in mafic melts. *Geochim. et Cosmochim. Acta* **97**, 1-23.

Ihinger P. D., Hervig R. L. and McMillan P. F. (1994) Analytical methods for volatiles in glasses. In: Carroll M.R., Holloway J.R. (eds) Volatiles in magmas. (Review in mineralogy) Mineral. Soc. Am., Washington, DC, 30, pp 67-121.

Ildefonse P., Calas G., Flank A. M. and Lagarde P. (1995) Low Z elements (Mg, Al, and Si) K-edge X-ray absorption spectroscopy in minerals and disordered systems. *Nucl. Instrum. Methods Phys. Res. B Beam Interact. Mater. Atoms* **97**, 172–175.

Iuga D., Morais C., Gan Z., Neuville D. R., Cormier L. and Massiot D. (2005) NMR Heteronuclear Correlation between quadrupolar nuclei in solids. *J. Am. Chem. Soc.* **127**, 11540-11541.

Jakobsson S. (1997) Solubility of water and carbon dioxide in an icelandite at 1400°C and 10 kilobars. *Contrib. Mineral. Petrol.* **127**, 129-135.

Jaworski A., Stevensson B., Pahari B., Okhotnikov K. and Edén M. (2012) Local structures and Al/Si ordering in lanthanum aluminosilicate glasses explored by advanced ^{27}Al NMR experiments and molecular dynamics simulations. *Phys. Chem. Chem. Phys.* **14**, 15866–15878.

Jaworski A., Stevenson B. and Eden M. (2015) Direct ^{17}O NMR experimental evidence for Al–NBO bonds in Si-rich and highly polymerized aluminosilicate glasses. *Phys. Chem. Chem. Phys.* **17**, 18269-18272.

Kalampounias A. G., Nasikas N. K. and Papatheodorou G. N. (2009) Glass formation and structure in the $MgSiO_3$–Mg_2SiO_4 pseudobinary system: from degraded networks to ionic like glasses. *J. Chem. Phys.* **131**, 114513-114521.

Katz A. K., Glusker J. P., BeeBe S. A., Bock C. W. (1996) Calcium Ion Coordination: A Comparison with That of Beryllium, Magnesium, and Zinc. *J. Am. Chem. Soc.* **118**, 5752-5763.

Kelsey K. E., Allwardt J. R. and Stebbins J. F. (2008) Ca-Mg mixing in aluminosilicate glasses: An investigation using the ^{17}O MAS and 3QMAS and ^{27}Al MAS NMR. *J. Non-Cryst. Solids* **354**, 4644-4653.

Kelsey K. E., Stebbins J. F., Singer D. M., Brown G. E. J., Mosenfelder J. L. and Asimow P. D. (2009) Cation field strength effects on high pressure aluminosilicate glass structure: Multinuclear NMR and La XAFS results. *Geochim. et Cosmochim. Acta* **73**, 3914-3933.

King P. L., Vennemann T. W., Holloway J. R., Hervig R. L., Lowenstern J. B. and Forneris J. F. (2002) Analytical techniques for volatiles: A case study using intermediate (andesitic) glasses. *Am. Mineral.* **87**, 1077-1089.

Kjarsgaard B. A., Pearson D. G., Tappe S., Nowell G. M. and Dowall D. P. (2009) Geochemistry of hypabyssal kimberlites from Lac de Gras, Canada: Comparisons to a global database and applications to the parent magma problem. *Lithos* **1125**, 236-248.

Kjeldsen J., Smedskjaer M. M., Mauro J. C., Youngman R. E., Huang L. and Yue Y. (2013) Mixed alkaline earth effect in sodium aluminosilicate glasses. *J. Non-Cryst. Solids* **369**, 61-68.

Kohara S., Suzuya K., Takeuchi K., Loong C. -K., Grimstditch M., Weber J. K. R., Tangeman A. and Key S. (2004) Glass formation at the limit of insufficient network formers. *Science* **303**, 1649–1652.

Kohara S., Akola J., Morita H., Suzuya K., Weber J. K. R., Wilding M. C. and Benmore C. J. (2011) Relationship between topological order and glass forming ability in densely packed enstatite and forsterite composition glasses. *Proc. Nat. Acad. Sci.* **108**, 14780-14785.

Kohn S. C., Brooker R. A. and Dupree R. (1991) ^{13}C MAS NMR: A method for studying CO_2 speciation in glasses. *Geochim. et Cosmochim. Acta* **55**, 3879–3884.

Kopylova M. G., Matveev S. and Raudsepp M. (2007) Searching for parental kimberlite melt. *Geochim. et Cosmochim. Acta* **71**, 3616–3629.

Kroeker S. and Stebbins J. F. (2000) Magnesium coordination environments in glasses and minerals: new insight from high-field magnesium-25 MAS NMR. *Am. Mineral.* **85**, 1459–1464.

Kubicki J. D. and Stolper E. M. (1995) Structural roles of CO_2 and $[CO_3]^{2-}$ in fully polymerized, sodium aluminosilicate melts and glasses. *Geochim. et Cosmochim. Acta* **59**, 683–698.

Kubicki J. D. and Toplis M. J. (2002) Molecular orbital calculations on aluminosilicate tricluster molecules: Implications for the structure of aluminosilicate glasses. *Am. Mineral.* **87**, 668-678.

Lange R. and Carmichael I. S. E (1990) Thermodynamic properties of silicate liquids with emphasis on density, thermal expansion and compressibility. In J. Nicholls and J.K. Russell, Eds., Modern Methods of Igneous Petrology: Understanding Magmatic Processes, 24, p. 25–64. Reviews in Mineralogy, Mineralogical Society of America, Chantilly, Virginia.

Le Losq C., Neuville D. R., Moretti R. and Roux J. (2012) Determination of water content in silicate glasses using Raman spectrometry: Implications for the study of explosive volcanism. *Am. Mineral.* **97**, 779–790.

Lee, S. K. and Sung, S. (2008) The effect of network-modifying cations on the structure and disorder in peralkaline Ca-Na aluminosilicate glasses: O-17 3QMAS NMR Study. *Chem. Geol.* **256**, 326-333.

Lee S. K. and Stebbins J. F. (2002) The extent of inter-mixing among framework units in silicate glasses and melts. *Geochim. et Cosmochim. Acta* **66**, 303–309.

Lee S. K. and Stebbins J. F. (2003) The distribution of Na ions in aluminosilicate glasses: a high-field ^{23}Na MAS and 3QMAS NMR study. *Geochim. et Cosmochim. Acta* **67**, 1699–1709.

Lee S. K. and Stebbins J. F. (2006) Disorder and the extent of polymerization in calcium silicate and aluminosilicate glasses: O-17 NMR results and quantum chemical molecular orbital calculations. *Geochim. et Cosmochim. Acta* **70**, 4275–4286.

Lee S. K. and Stebbins J. F. (2009) Effects of the degree of polymerization on the structure of sodium silicate and aluminosilicate glasses and melts: An ^{17}O NMR study. *Geochim. et Cosmochim. Acta* **73**, 1109-1139.

Lee S. K., Cody G. D., Fei Y. and Mysen B. O. (2004) The nature of polymerization and properties of silicate glasses and melts at high pressure. *Geochim. et Cosmochim. Acta* **68**, 4203–4214.

Lee S. K., Cody G. D. and Mysen B. O. (2005) Structure and the extent of disorder in quaternary (Ca–Mg and Ca–Na) aluminosilicate glasses and melts. *Am. Mineral.* **90**, 1393–1401.

Lee S. K.; Kim H. N.; Lee B. H.; Kim H. I.; Kim E. J. (2010) Nature of chemical and topological disorder in borogermanate glasses: insights from B-11 and O-17 Solid-State NMR and quantum chemical calculations. *J. Phys. Chem. B.* **114**, 412-420.

Lee S. K., Kim H. I., Kim E. J., Mun K. Y. and Ryu S. (2015) The Extent of Disorder in Magnesium Aluminosilicate Glasses: Insights from ^{27}Al and ^{17}O NMR. *J. Phys. Chem. C* accepted.

Lesne P., Scaillet B., Pichavant M. and Beny J. M. (2011b) The carbon dioxide solubility in alkali basalts: an experimental study. *Contrib. Mineral. Petrol.* **162**, 153–168. http://dx.doi.org/ 10.1007/s00410-010-0585-0.

Li D., Peng M. S. and Murata T. (1999) Coordination and local structure of magnesium in silicate minerals and glasses: Mg K-edge XANES study. *Can. Mineral.* **37**, 199–206.

Long D. A. (2002). The Raman Effect: A Unified Treatment of the Theory of Raman Scattering by Molecules, pp. 598. Wiley, New York.

Maekawa H., Maekawa T., Kawamura K. and Yokokawa T. (1991) The structural groups of alkali silicate glasses determined from ^{29}Si MAS NMR. *J. Non-Cryst. Solids* **127**, 53-64.

Malfait W. J., Halter W. E., Morizet Y., Meier B. H. and Verel R. (2007) Structural control on bulk melt properties: single and double quantum ^{29}Si NMR spectroscopy on alkali–silicate glasses. *Geochim. et Cosmochim. Acta* **71**, 6002–6018.

Mandeville C. W., Webster J. D., Rutherford M. J., Taylor B. E., Timbal A. and Faure K. (2002) Determination of molar absorptivities for infrared absorption bands of H_2O in andesitic glasses. *Am. Mineral.* **87**, 813-821.

Martin L. H. J., Schmidt M. W., Mattsson H. B. and Günther D. (2013) Element partitioning between immiscible carbonatite and silicate melts for dry and H_2O-bearing systems at 1–3 GPa. *J. Petrol.* **54**, 2301–2338.

Massuyeau M., Gardés E., Morizet Y. and Gaillard F. (2015) A model for the ac-tivity of silica along the carbonatite–kimberlite–melilitite–basanite melt com-positional joint. *Chem. Geol.* **418**, 206-216.

Mattey D. P., Taylor W. R., Green D. H. and Pillinger C. T. (1990) Carbon isotopic fractionation between CO_2 vapour, silicate and carbonate melts: an experimental study to 30 kbar. *Contrib. Mineral. Petrol.* **104**, 492-505.

Mercier M., Di Muro A., Giordano D., Métrich N., Lesne P., Pichavant M., Scaillet B. and Clocchiatti R. (2009) Influence of glass polymerisation and oxidation on micro-Raman water analysis in alumino-silicate glasses. *Geochim. et Cosmochim. Acta* **73**, 197-217.

Mitchell R. H. (2008) Petrology of hypabyssal kimberlites: Relevance to primary magma compositions. *J. Volc. Geotherm. Res.* **174**, 1-8.

Morizet Y., Brooker R. A. and Kohn S. C. (2002) CO_2 in haplo-phonolite Melt: Solubility, speciation and carbonate complexation. *Geochim. et Cosmochim. Acta* **66**, 1809-1820.

Morizet Y., Paris M., Gaillard F. and Scaillet B. (2010) C-O-H fluid solubility in haplobasalt under reducing conditions: An experimental study. *Chem. Geol.* **279**, 1-16.

Morizet Y., Brooker R. A., Iacono-Marziano G. and Kjarsgaard B. (2013) Quantification of CO_2 dissolved in silicate glasses of various compositions with Micro-Raman spectroscopy. *Am. Mineral.* **98**, 1788-1802.

Morizet Y., Paris M., Gaillard F. and Scaillet B. (2014a) Carbon dioxide in silica undersaturated melt. Part I: the effect of mixed alkalis (K and Na) on CO_2 solubility and speciation. *Geochim. et Cosmochim. Acta* **141**, 45–61.

Morizet Y., Vuilleumier R. and Paris M. (2015) A NMR and molecular dynamics study of CO_2-bearing basaltic melts and glasses. *Chem. Geol.* **418**, 89-103.

Moussallam Y., Morizet Y., Massuyeau M., Laumonier M. and Gaillard F. (2015) CO_2 solubility in kimberlite melts. *Chem. Geol.* **418**, 198-205.

Moussallam Y., Florian P., Corradini D., Morizet Y., Sator N., Vuilleumier R., Guillot B., Iacono-Marziano G., Schmidt B. C. and Gaillard F. (2016a) The molecular structure of melts along the carbonatite–kimberlite–basalt compositional joint: CO_2 and polymerization. *Earth Planet. Science Lett.* **434**, 129-140.

Moussallam Y., Morizet Y. and Gaillard F. (2016b) H_2O-CO_2 solubility in low SiO_2-melt and the unique mode of kimberlite degassing and emplacement. *Earth Planet. Science Lett.* **447**, 151-160.

Murdoch J. B., Stebbins J. F. and Carmichael I. S. E. (1985) High resolution ^{29}Si NMR study of silicate and aluminosilicate glasses: the effect of network modifying cations. *Am. Mineral.* **70**, 332–343.

Mysen B. O. and Seitz M. G. (1975) Trace element partitioning determined by beta-track mapping---an experimental study using carbon and samarium as examples. *J. Geophys. Res.* **80**, 2627-2635.

Mysen B. O., Virgo D. and Scarfe C. M. (1980) Relations between the anionic structure and viscosity of silicate melts – a Raman spectroscopic study. *Am. Mineral.* **65**, 690-710.

Mysen B. O., Virgo D. and Seifert F. A. (1982) The structure of silicate melts; implications for chemical and physical properties of natural magma. *Rev. Geophys. Space Phys.* **20**, 353–383.

Mysen B. O. (1988) Structure and properties of silicate melts. Developments in Geochemistry, vol. 4. Elsevier, Amsterdam, 354 pp.

Mysen B. O. (1990) Effect of pressure, temperature, and bulk composition on the structure and species distribution in depolymerized alkali aluminosilicate melts and quenched melts. *J. Geophys. Res. B* **95**, 15733-15744.

Mysen B. O. (1999) Structure and properties of magmatic liquids: From haplobasalt to haploandesite. *Geochim. et Cosmochim. Acta* **63**, 95–112.

Nasikas N. K., Chrissanthopoulos A., Bouropoulos N., Sen S. and Papatheodorou G. N. (2011) Silicate glasses at the ionic limit: alkaline-earth sub-orthosilicates. *Chem. Mater.* **23**, 3692–3697.

Nasikas N. K., Edwards T. G., Sen S. and Papatheodorou G. N. (2012) Structural characteristics of novel Ca–Mg orthosilicate and suborthosilicate glasses: results from ^{29}Si and ^{17}O NMR spectroscopy. *J. Phys. Chem. B* **116**, 2696–2702.

Nesbitt W. H., Bancroft M. G., Henderson G. S., Sawyer R. and Secco R. A. (2015) Direct and indirect evidence for free oxygen (O^{2-}) in MO-silicate glasses and melts (M = Mg, Ca, Pb). *Am. Mineral.* **100**, 2566-2578.

Neuville D. R. and Mysen B. O. (1996) Role of the Al in the silicate network: in situ, high temperature study of glasses and melts on the join SiO_2-$NaAlO_2$. *Geochim. et Cosmochim. Acta* **60(10)**, 1727-1737.

Neuville D. R. and Richet P. (1991) Viscosity and mixing in molten (Ca, Mg) pyroxenes and garnets. *Geochim. et Cosmochim. Acta* 55, 1011–1019.

Ohlhorst S., Behrens H. and Holtz F. (2001) Compositional dependence ofmolar absorptivities of near-infrared OH⁻ and H_2O bands in rhyolitic to basaltic glasses. *Chem. Geol.* **174**, 5–20.

Papale P., Moretti R. and Barbato D. (2006) The compositional dependence of the saturation surface of H_2O +CO_2 fluids in silicate melts. *Chem. Geol.* **229**, 78–95.

Pedone A., Gambuzzi E. and Menziani M. C. (2012) Unambiguous description of the oxygen environment in multicomponent aluminosilicate glasses from ^{17}O Solid State NMR computational spectroscopy. *J. Phys. Chem. C* **116**, 14599-14609.

Russell J. K., Porritt L. A., Lavallée Y. and Dingwell D. B. (2012) Kimberlite ascent by assimilation-fuelled buoyancy. *Nature* **481**, 352–356.

Sawyer R., Nesbitt H.W., Bancroft M. G., Thibault Y. and Secco R. A. (2015) Spectroscopic studies of oxygen speciation in potassium silicate glasses and melts. *Can. J. Chem.* **93**, 60-73.

Sen S., Gjersing E. L., Maekawa H., Noda Y., Ando M., Tansho M., Shimizu T., Klyuev V. P. and Pevzner B. Z. (2009) Atomic structure of BeO-B_2O_3-Al_2O_3 glasses: ^{11}B and ^{27}Al MAS NMR spectroscopy at 21.8 Tesla. *Phys. Chem. Glasses* **50**, 262-266.

Sharma S. K. (1979) Structure and solubility of carbon dioxide in silicate glasses of diopside and sodium melilite compositions at high pressures from Raman spectroscopic data. In: Yearbook Carnegie Inst. Wash., pp.532–537.

Sharygin I. S., Litasov K. D., Shatskiy A., Golovin A. V., Ohtani E. and Pokhilenko N. P. (2015) Melting phase relations of the Udachnaya-East Group-I kimberlite at 3.0–6.5 GPa: Experimental evidence for alkali-carbonatite composition of primary kimberlite melts and implications for mantle plumes. *Gondwana Res.* **28**, 1391-1414.

Shimoda K., Tobu Y., Hatakeyama M., Nemoto T. and Saito K. (2007) Structural investigation of Mg local environments in silicate glasses by ultra-high field ^{25}Mg 3QMAS NMR spectroscopy. *Am. Mineral.* **92**, 695-698.

Shimoda K., Nemoto T. and Saito K. (2008a) Local Structure of Magnesium in Silicate Glasses: A ^{25}Mg 3QMAS NMR Study. *J. Phys. Chem. B* **112**, 6747-6752.

Shimoda K., Tobu Y., Kanehashi K., Nemoto T. and Saito K. (2008b) Total understanding of the local structures of an amorphous slag: Perspective from multi-nuclear (^{29}Si, ^{27}Al, ^{17}O, ^{25}Mg, and ^{43}Ca) solid-state NMR. *J. Non-Cryst. Solids* **354**, 1036-1043.

Shishkina T. A., Botcharnikov R. E., Holtz F., Almeev R. R. and Portnyagin M. V. (2010) Solubility of H_2O- and CO_2-bearing fluids in tholeiitic basalts at pressures up to 500 MPa. *Chem. Geol.* **277**, 115-125.

Shishkina T., Botcharnikov R. E., Holtz F., Almeev R. R., Jazwa A. M. and Jakubiak A. A. (2014) Compositional and pressure effects on the solubility of H_2O and CO_2 in mafic melts. *Chem. Geol.* **388**, 112-129.

Smith M. E., Steuernagel S. and Whitfield H. J. (1995) [17]O Mafic-angle spinning nuclear magnetic resonance of $CaCO_3$. *Solid State Nuc. Magn. Res.* **4**, 313-316.

Sokol A. G. and Kruk A. N. (2015) Conditions of kimberlite magma generation: experimental constraints. *Russian Geol. Geophys.* **56**, 245-259.

Sokol A. G., Khokhryakov A. F. and Palyanov Y. N. (2015) Composition of primary kimberlite magma: constraints from melting and diamond dissolution experiments. *Contrib. Mineral. Petrol.* **170**, 26-44.

Sparks R. S. J., Baker L., Brown R. J., Field M., Schumacher J., Stripp G. and Walkers A. (2006) Dynamical constraints on kimberlite volcanism. *J. Volc. Geotherm. Res.* **155**, 18-48.

Stebbins J. F., Oglesby J. V. and Xu Z. (1997) Disorder among network-modifier cations in silicate glasses: new constraints from triple-quantum ^{17}O NMR. *Am. Mineral.* **82**, 1116–1124.

Stebbins J. F., Oglesby J. V. and Kroeker S. (2001) Oxygen triclusters in crystalline $CaAl_4O_7$ (grossite) and in calcium aluminosilicate glasses: ^{17}O NMR. *Am. Mineral.* **86**, 1307-1311.

Tabira Y. (1996) Local structure around oxygen atoms in $CaMgSi_2O_6$ glass by O K-edge EXELFS. *Mater. Sci. Eng. B* **41**, 63–66.

Thibault Y. and Holloway J. R. (1994) Solubility of CO_2 in a Ca-rich leucitite: Effects of pressure, temperature and oxygen fugacity. *Contrib. Miner. Petrol.* **116**, 216-224.

Thompson L. M. and Stebbins J. F. (2011) Non-bridging oxygen and high-coordinated aluminum in metaluminous and peraluminous calcium and potassium aluminosilicate glasses: High-resolution ^{17}O and ^{27}Al MAS NMR results. *Am. Mineral.* **96**, 841-853.

Toplis M. J., Dingwell D. B. and Lenci T. (1997) Peraluminous viscosity maxima in Na_2O-Al_2O_3-SiO_2 liquids: the role of triclusters in tectosilicate melts. *Geochim. et Cosmochim. Acta* **61**, 2605-2612.

Tossell J. A. (1995) Calculation of the ^{13}C NMR shieldings of the CO_2 complexes of aluminosilicates. *Geochim. et Cosmochim. Acta* **59**, 2199–1305.

Verweij H., Van Den Boom H., Breemer R. E. (1977) Raman scattering of carbon-ate ions dissolved in potassium silicate glasses. *J. Am. Ceram. Soc.* **60**, 529–534.

Walter M. J. (1998) Melting of garnet peridotite and the origin of komatiites and depleted lithosphere. *J. Petrol.* **39**, 29–60.

White W. B. (1974) The carbonate minerals. In: The Infrared Spectra of Minerals. In: Mineralogical Society of London Monograph, pp.227–284.

Wilding M. C., Benmore C. J., Tangeman J. A. and Sampath S. (2004) Coordination changes in magnesium silicate glasses. *Europhys. Lett.* **67**, 212–218.

Wilding M., Guthrie M., Kohara S., Bull C. L., Akola J. and Tucker M. G. (2012) The structure of MgO–SiO_2 glasses at elevated pressure. *J. Phys. Condens. Matter* **24**, 225403-225414.

Figure caption:

Figure 1: Raman spectra in the 750-1250 cm^{-1} showing the symmetric stretch of the CO_3^{2-} molecules (~1080 cm^{-1}) and the symmetric stretch of the aluminosilicate network. The CO_2 solubility is reported next to each spectrum and has been determined using the method of Morizet et al. (2013). Spectra are shown for X1 to X3 silicate glasses (A and B) with XMg changing from 0.24 to 0.72; for RB8 and HK silicate glasses with XMg from 0 to 0.6, at 0.5 and 1.5 GPa (C and D). Typical Raman spectrum simulation to determine CO_2 solubility is shown underneath the bottom spectrum. Simulations were conducted with five Gaussian lines and are reported for all samples in the Supplementary material 1 and 2.

Figure 2: ^{17}O MAS NMR spectra acquired on RB8E, HK and XE2 compositions. The spectra show evidences for bridging oxygens species T-O^{BO}-T, for non-bridging oxygen species Ca O^{NBO} and Mg O^{NBO}. An additional signature at ~+140 ppm is attributed to C-related species and has been assigned to CO_3^{2-} species. A weak additional signal is also visible at ~-20 ppm and is attributed to oxygen species in tricluster configuration (O$^{III\ BO}$).
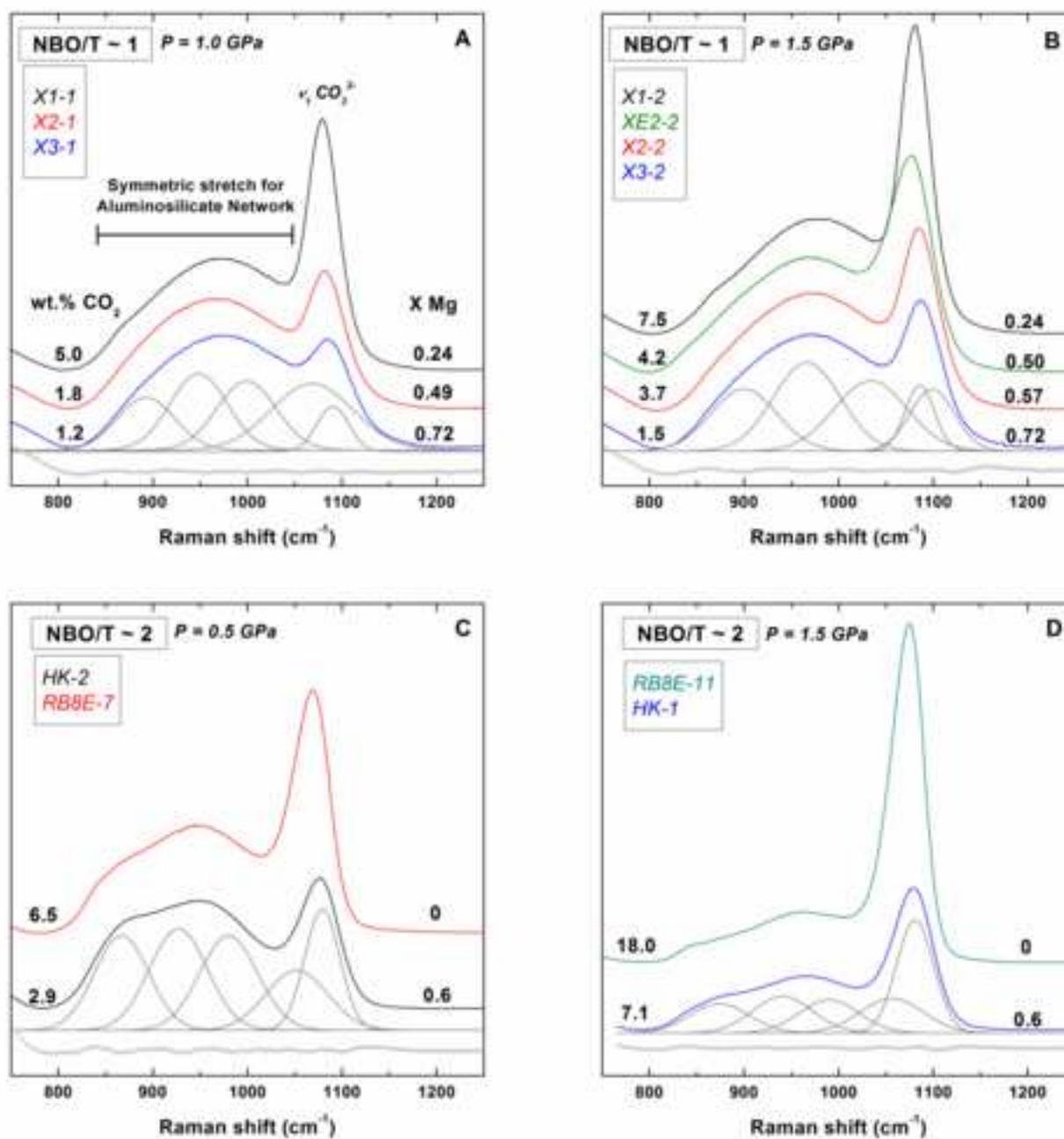
Figure 3: Change in CO_2 solubility as a function of the XMg calculated from the glass chemical compositions. Data are represented as a function of pressure between 0.5 and 1.5 GPa. The experimental CO_2 solubility is represented as a function of the degree of polymerization: NBO/T ~ 1 (Figure 3A) and NBO/T ~ 2 (Figure 3B). For a given category, increasing the XMg induces a decrease in CO_2 solubility. The error bars on the XMg is within the point and the error on CO_2 solubility is taken as 10% in relative to the value. CO_2 solubility data from Brooker et al. (2001a) obtained at 1.5 GPa have been added. Those data
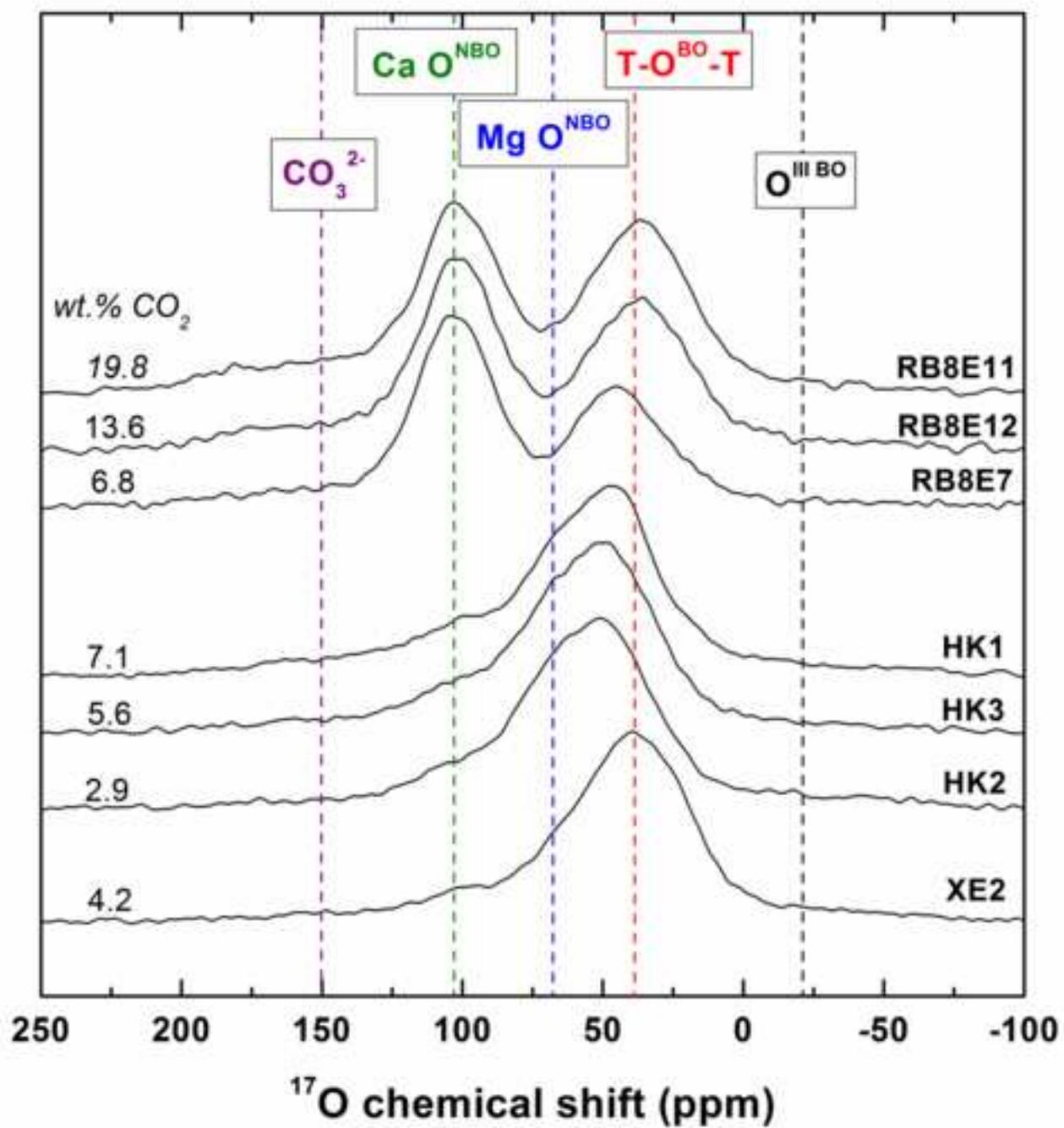
points have XMg values from 0 to 0.26 and NBO/T ~ 2 and can be compared to the CO_2

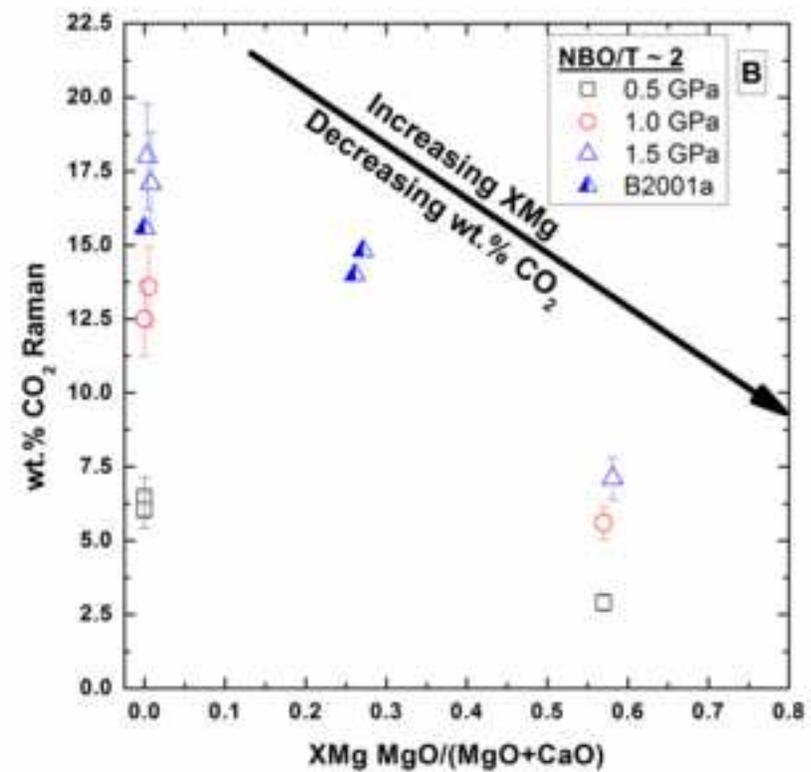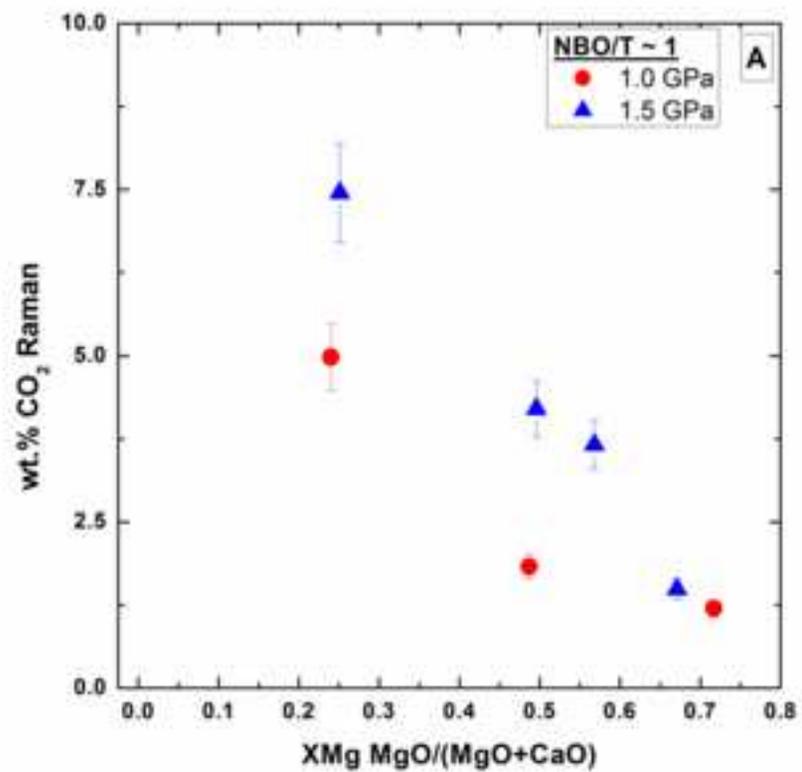solubility results obtained on RB8 and HK at identical pressure.

Figure 4: Typical spectral deconvolution of ^{17}O NMR spectra for RB8E7 (A, 6.5 wt.% CO_2),

HK-1 (B, 7.1 wt.% CO_2) and XE2-2 (C, 4.2 wt.% CO_2). Results of the deconvolution are

reported in Table 2. ^{17}O NMR spectra were decomposed with four Gaussian lines for RB8E

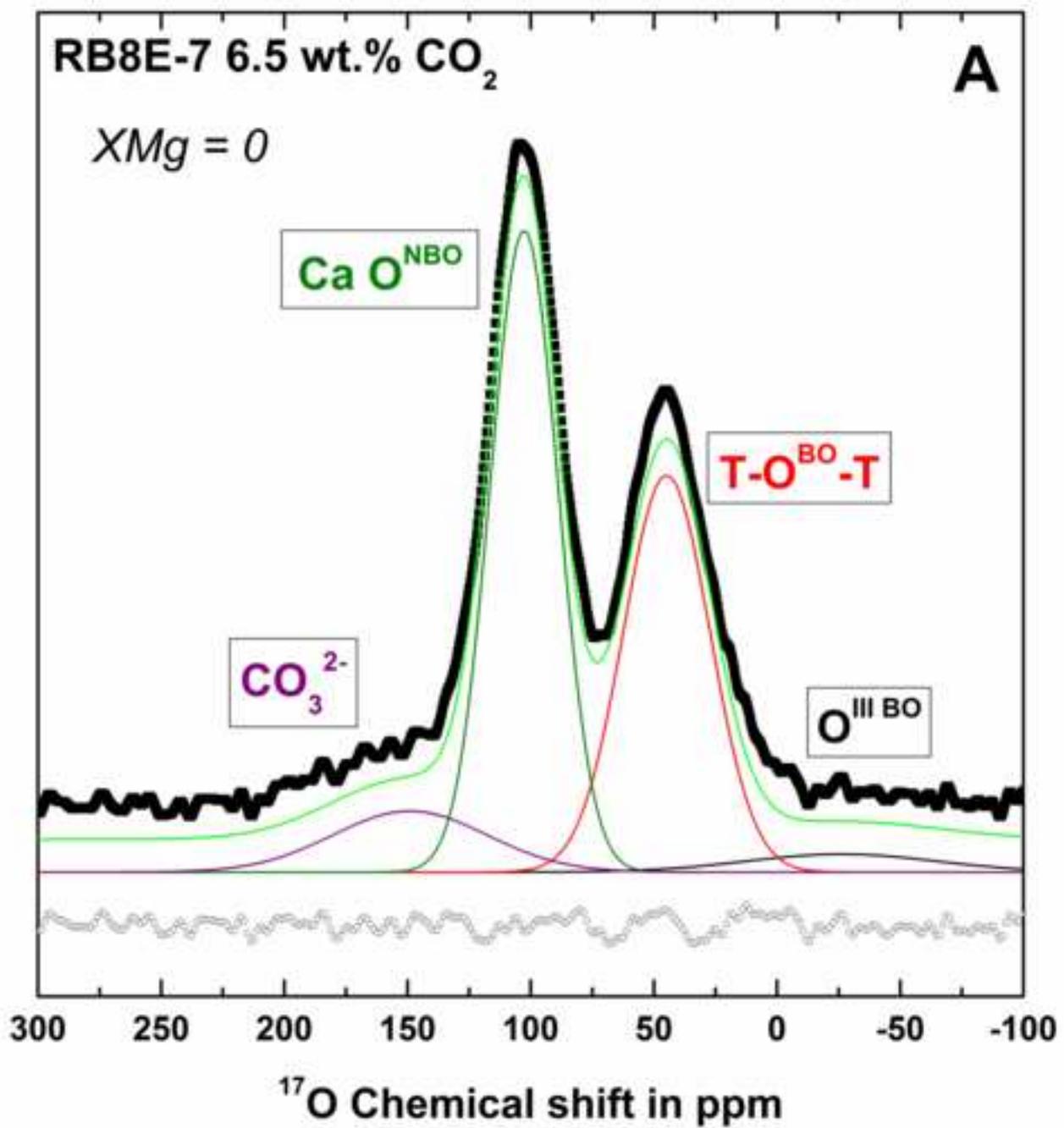and five Gaussian lines for HK-1 and XE2-2.

Figure 5: CO_2 content XCO_3^{2-} measured by ^{17}O NMR (see Table 2 for the XCO_3^{2-} values

from the deconvolution) as a function of XCO_2 calculated from the major element

composition and the measured wt.% CO_2 by Raman (see Table 1). A linear function has been

fitted through the data points.

Figure 6: wt.% CO_2 as a function of Melt IFS calculated from Eq. 3 using the silicate melt

chemical composition and the ionic field strength (z_i/r_i^2, see text for detail). We show

experimental CO_2 solubility data points collected from the literature: Brey and Green (1976);

Mattey et al. (1990); Brey et al. (1991); Pan et al. (1991); Thibault and Holloway (1994);

Jakobsson (1997); Brooker et al. (2001a, b; 2011), Brooker and Kjarsgaard (2011); Morizet et

al. (2002); Shishkina et al. (2010, 2014); Morizet et al. (2015); Moussallam et al. (2015,

2016b). Data points have been categorized as a function of pressure between 0.5 and 2.0 GPa.

We also reported the CO_2 content and Melt IFS measured in natural kimberlites using the

compilation of natural data from Kjarsgaard et al. (2009). The entire dataset (experimental

and natural) is provided in Supplementary material 2.

Figure 1

Figure 2

Figure 2

Figure 3

Figure 4A

HK-1 7.1 wt.% CO_2

$XMg = 0.58$

B

$T-O^{BO}-T$

$Mg\,O^{NBO}$

$Ca\,O^{NBO}$

CO_3^{2-}

$O^{III\,BO}$

^{17}O Chemical shift in ppm

Figure 4C. XE2-2 4.2 wt.% CO_2, $XMg = 0.50$. ^{17}O Chemical shift in ppm. Labeled components: CO_3^{2-}, Ca O^{NBO}, Mg O^{NBO}, T-O^{BO}-T, $O^{III\ BO}$.

Figure 5

Legend:
- ■ RB8E
- ● HK
- ▲ XE2

$XCO_3^{2-\ 17}O\ NMR = 0.838 \times XCO_2^{Raman}$

Y-axis: $XCO_3^{2-\ 17}O\ NMR$
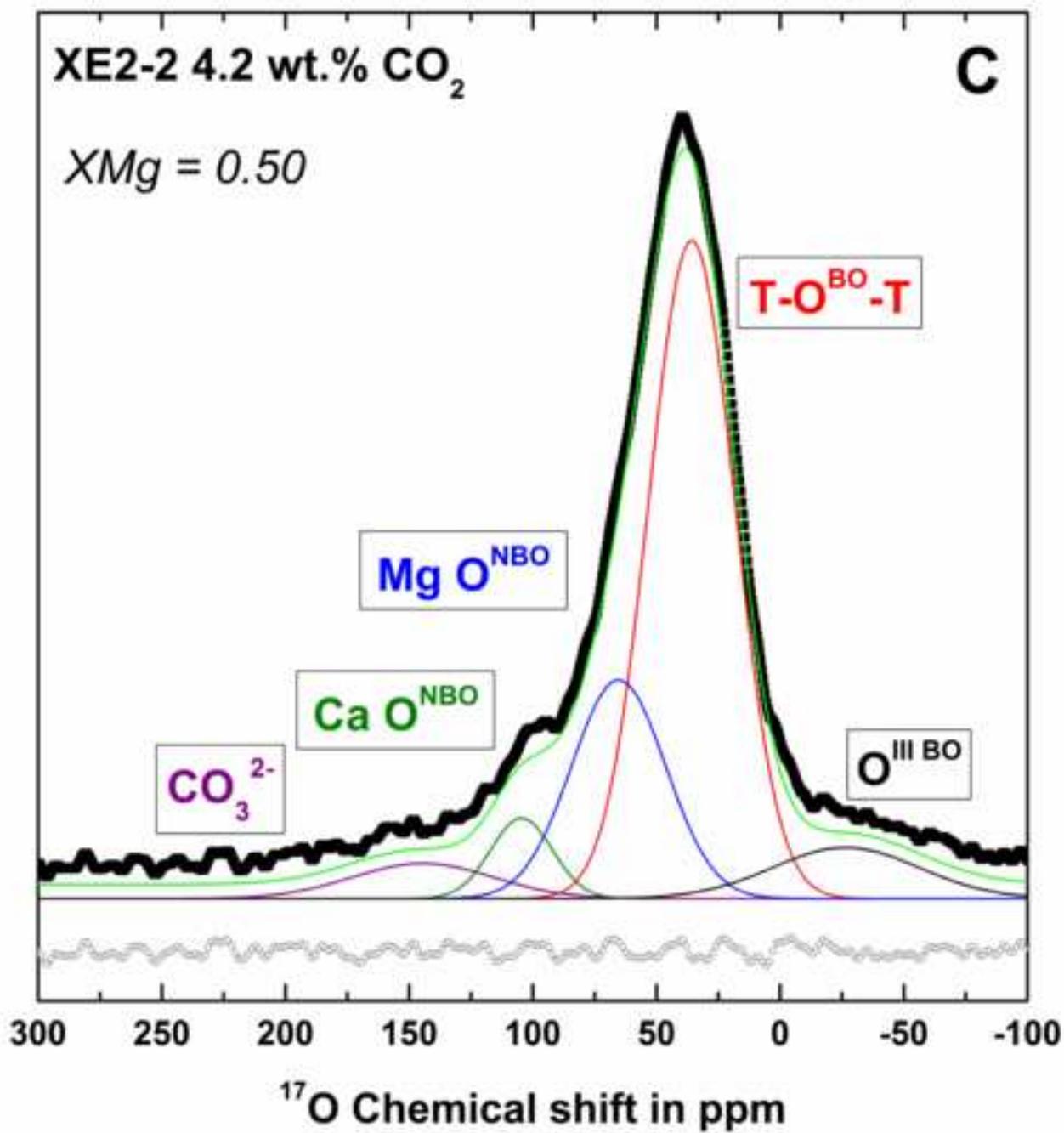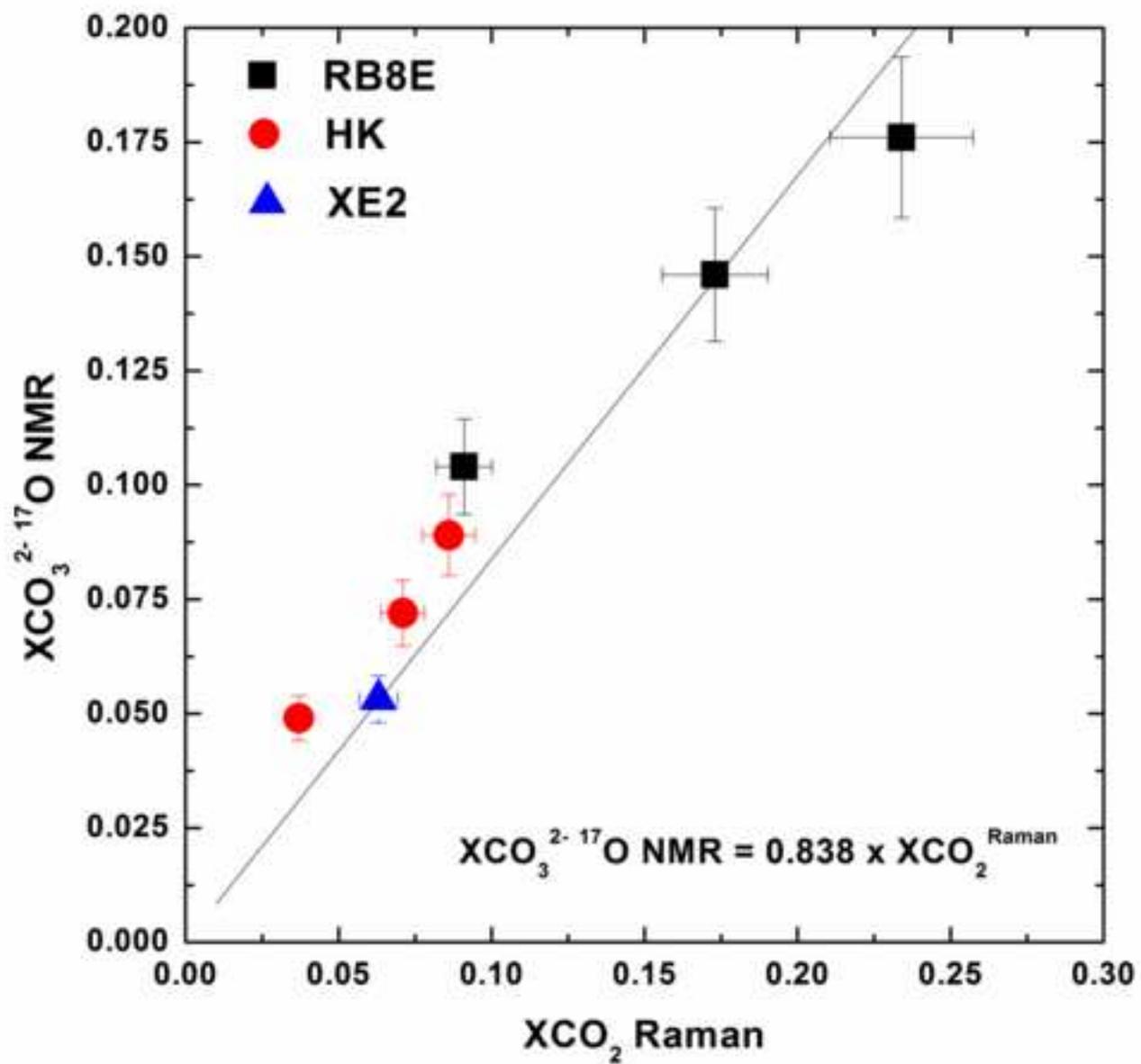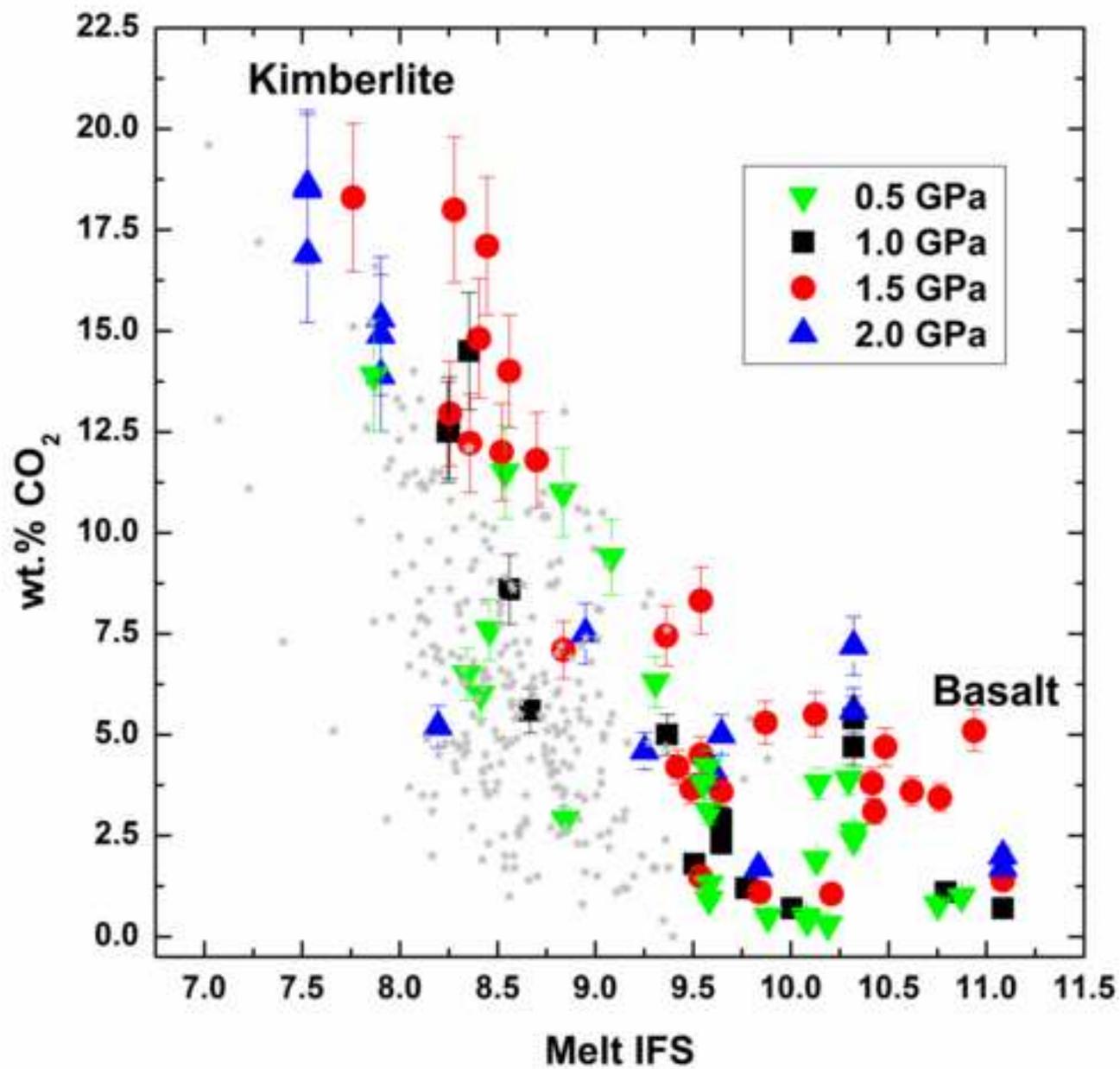
X-axis: $XCO_2\ Raman$

Figure 6

Table 1: Experimental conditions, glass compositions and volatile contents.

Sample	Theoretical NBO/T ~ 1							Theoretical NBO/T ~ 2								
	X1-1	X2-1	X3-1	X1-2	X2-2	XE2-2[a]	X3-2	RB8-2	RB8E-7[a]	HK-2[a]	RB8E-12[a]	RB8-14	HK-3	RB8-1	RB8E-11[a]	HK-1[a]
Pressure (GPa)	1.0	1.0	1.0	1.5	1.5	1.5	1.5	0.5	0.5	0.5	1.0	1.0	1.0	1.5	1.5	1.5
Major element composition in wt.% determined by EPMA[b]																
SiO_2	41.2 (3)	43.5 (3)	46.5 (3)	39.7 (3)	42.3 (2)	40.6 (4)	43.1 (4)	33.2 (3)	33.3 (4)	40.1 (3)	30.3 (6)	30.3 (3)	37.2 (4)	31.3 (5)	29.7 (5)	40.2 (6)
Al_2O_3	13.9 (3)	16.4 (2)	17.0 (3)	14.2 (2)	15.6 (3)	14.8 (2)	16.1 (2)	9.8 (2)	8.7 (2)	4.4 (1)	8.1 (2)	8.5 (1)	4.2 (1)	9.3 (2)	8.0 (1)	4.3 (1)
MgO	6.0 (1)	12.5 (1)	17.9 (1)	6.0 (1)	14.6 (1)	12.6 (1)	17.6 (1)	0.2 (0)	0.0 (1)	21.3 (1)	0.1 (0)	0.1 (1)	21.8 (2)	0.2 (0)	0.1 (0)	21.9 (2)
CaO	26.7 (2)	18.4 (1)	9.9 (1)	25.1 (2)	15.5 (1)	17.8 (1)	12.0 (1)	40.4 (2)	41.8 (3)	22.3 (2)	39.8 (3)	39.7 (3)	21.4 (2)	37.9 (5)	38.6 (3)	22.0 (2)
Na_2O	4.8 (1)	5.0 (1)	5.5 (1)	4.8 (1)	5.1 (1)	4.8 (1)	5.2 (1)	4.9 (1)	5.7 (3)	4.5 (1)	4.8 (1)	4.9 (1)	4.5 (1)	4.4 (2)	4.6 (1)	4.5 (1)
Total	92.6	95.8	96.8	89.8	93.1	90.8	94.0	88.5	89.5	92.6	83.1	83.4	92.8	83.1	81.0	92.9
XMg[c]	0.24	0.49	0.72	0.25	0.57	0.50	0.67	0	0	0.57	0	0	0.59	0	0	0.58
NBO/T[d]	1.2	1.1	1.0	1.1	1.1	1.2	1.1	1.9	2.1	2.5	2.2	2.1	2.7	1.9	2.1	2.6
Volatile concentrations in wt.%																
CO_2 initial	11	12	11	11	12	10	11	40	40	18	18	40	18	40	32	18
CO_2 Raman[e]	5.0	1.8	1.2	7.5	3.7	4.2	1.5	6.0	6.5	2.9	12.6	12.5	5.6	17.1	18.0	7.1
CO_2 Flash[f]		2.2 ±0.7			3.9 ±0.2			8.9 ±0.3				11.5 ±0.2		14.2 ±0.1		
H_2O FTIR[g]	0.4	0.2	0.4	1.2	0.7	1.0	0.6	0.6	0.7	1.0	1.5	0.4	0.8	0.6	0.9	0.8

[a] Those glass samples were prepared from ^{17}O isotopically enriched $Si^{17}O_2$ and $Al_2^{17}O_3$ oxides.

[b] The major element concentrations by EPMA was obtained on more than 15 analyses on each sample. The error is indicated between brackets (last digit) and represents the standard deviation of the analyses on each oxide.

[c] The XMg is defined as molar ratio MgO/(MgO+CaO).

[d] The NBO/T corresponds to the concentration of Non-Bridging Oxygen per Tetrahedron and is calculated from the chemical composition (Mysen, 1988, 1990). The NBO concentration corresponds to the excess negative charges brought by the oxygen in each oxide. This excess negative charge is subsequently divided by the positive charges on tetrahedra which is represented by the molar concentration of Si^{4+} and Al^{3+}.

[e] The CO_2 solubility has been determined using the method of Morizet et al. (2013) and using the derived CO_3/HF value obtained from the deconvolution of the Raman spectra. The linear relationship has been re-evaluated and is wt.% CO_2 = 13.5 x CO_3/HF. The typical error on the CO_2 solubility is 10% in relative to the value.

[f] Elemental analyses have been conducted on a few glass samples, not enriched in ^{17}O isotope. The error reported corresponds to the standard deviation calculated from replicated measurements.

[g] The H_2O content was determined by FTIR, summing the contribution of the OH^- and H_2O^{mol} vibrational peaks at 4500 and 5200 cm^{-1}, respectively. The error does not exceed ±0.2 wt.% H_2O and corresponds to the standard deviation obtained on the replicated measurements.

Table 2: Parameters derived from the deconvolution of the ^{17}O NMR spectra using Gaussian lines.

	RB8E7 6.5 wt.% CO_2	RB8E12 12.6 wt.% CO_2	RB8E11 18.0 wt.% CO_2	HK-2 2.9 wt.% CO_2	HK-3 5.6 wt.% CO_2	HK-1 7.1 wt.% CO_2	XE2-1 4.2 wt.% CO_2
T-O^{BO}-T with T = Si and/or Al							
δ_{iso} (ppm)	44.8	37.6	37.6	47.7	41.7	44.7	35.7
FWHM (ppm)	35.1	37.7	37.7	37.5	31.4	33.2	34.7
% area	37.9	42.9	44.7	52.4	45.5	43.1	59.8
O$^{BO\,III}$ Triclusters							
δ_{iso} (ppm)	-26.1	-29.4	-26.4	-21.3	-14.5	-14.8	-26.6
FWHM (ppm)	77.6	54.6	45.1	59.3	54.5	71.3	59.4
% area	3.8	4.0	3.3	8.1	6.1	9.5	7.9
Ca O^{NBO}							
δ_{iso} (ppm)	102.7	100.8	100.3	106.3	101.4	105.6	104.5
FWHM (ppm)	27.5	28.0	28.6	25.0	31.5	30.2	24.9
% area	47.9	38.4	34.4	7.0	12.3	9.6	5.3
Mg O^{NBO}							
δ_{iso} (ppm)				69.8	65.8	67.5	65.3
FWHM (ppm)				37.1	31.6	38.3	38.1
% area				27.6	35.0	28.9	21.8
CO_3^{2-}							
δ_{iso} (ppm)	149.0	144.5	146.5	143.9	147.9	146.8	144.4
FWHM (ppm)	62.8	70.0	75.5	53.0	57.7	53.8	56.9
X $CO_3^{2-\,NMR}$ [a]	0.104	0.146	0.176	0.049	0.072	0.089	0.079
XCO_2 Raman [b]	0.091	0.173	0.234	0.037	0.071	0.086	0.063

[a] The X$CO_3^{2-\,NMR}$ is calculated from the ratio between the CO_3^{2-} peak area divided by the total area of the O species contributions.

[b] The XCO_2 Raman is calculated from the wt.% CO_2 determined by Raman spectroscopy and the major element glass composition reported in Table 1.